Emerin oligomerization and nucleoskeletal coupling at the nuclear envelope regulate nuclear mechanics against stress

Anthony Fernandez[1], Markville Bautista[2] and Fabien Pinaud[1,2,3*]

[1]Department of Biological Sciences, University of Southern California, 1050 Childs Way, Los Angeles, CA 90089, USA.
[2]Department of Chemistry, University of Southern California, 1050 Childs Way, Los Angeles, CA 90089, USA.
[3]Department of Physics and Astronomy, University of Southern California, 1050 Childs Way, Los Angeles, CA 90089, USA.

*Correspondence should be addressed to F.P. (pinaud@usc.edu)

Abstract

Emerin is an integral membrane protein of the nuclear envelope that participates in the maintenance of nuclear shape. When mutated or absent, emerin causes X-linked Emery-Dreifuss muscular dystrophy (EDMD). To define how emerin takes parts in molecular scaffolding at the nuclear envelope and helps protect the nucleus against mechanical stress, we established its nanoscale spatial organizations using single molecule tracking and super-resolution microscopy. We show that emerin monomers form localized oligomeric nanoclusters that are stabilized by both lamin A/C and the LINC complex protein SUN1 at the inner nuclear membrane. Interactions of emerin with nuclear actin and BAF additionally modulate its lateral mobility and its ability to oligomerize. For nuclei subjected to mechanical challenges, we found that the mechanotransducing functions of emerin are coupled to changes in its oligomeric state, and that the incremental self-assembly of emerin determines nuclear shape adaptation against forces. We also show that the abnormal nuclear envelope deformations induced by EDMD emerin mutants stem from a defective formation of lamin A/C and LINC complex-stabilized emerin oligomers. These findings place emerin at the center of the molecular processes that regulate nuclear shape remodeling and maintain the structural integrity of the nuclear envelope in response to mechanical stress.

Introduction

Emerin is a conserved inner nuclear membrane (INM) protein that participates in the maintenance of the nuclear architecture by interacting with the nucleoskeletal lamina and elements of the linker of the nucleoskeleton and cytoskeleton (LINC) complex[1,2]. Emerin also contributes to tethering chromatin at the nuclear envelope by binding the DNA-bridging barrier-to-autointegration factor (BAF)[3] and it regulates the activity of chromatin compaction modulators[4]. Both the nucleoskeleton and the compaction state of chromatin contribute to the mechanical responses of nuclei to forces[5] and emerin is deemed a pivotal actor of mechanotransducing processes at the nuclear envelope[6]. When mutated or absent, emerin causes X-linked Emery-Dreifuss muscular dystrophy (EDMD)[7,8], a disease part of a larger of group of laminopathies[9] associated with structural perturbations of the nuclear envelope and its underlying lamina. While emerin is ubiquitously expressed, mutations in the *EMD* gene primarily affect cells exposed to extensive mechanical stress, such as skeletal and cardiac muscle cells. Emerin-null muscle tissues display deformed and disorganized nuclei, impaired myogenesis and improper muscle fiber formation, which participate in the muscle wasting and cardiac disease phenotypes of EDMD[10-12]. In non-muscle cells, loss of emerin also leads to altered nuclear envelope elasticity and increased nuclear fragility[13], impaired expression of mechanosensitive genes[14] and enhanced apoptosis after continuous mechanical strain[14]. EDMD phenotypes might stem from both an altered structural integrity of the nuclear envelope and modified gene expression profiles.

The structure of emerin and its binding to various partners have been extensively characterized in vitro[1]. Emerin is 254 amino acids (aa) long, with a N-terminal globular LAP2-emerin-MAN1 (LEM, aa: 1-45) domain, followed by a long intrinsically disordered region (IDR, aa: 46-222)[15] and a transmembrane domain close to the C-terminus (aa: 223-234) that allows anchoring to the nuclear envelope. Prominent binding partners of emerin include lamin A/C and lamin B[16-18], actin[19], BAF[20], nesprins and SUN proteins from the LINC complex[21,22], chromatin modification enzymes and other factors[1]. While binding of emerin to BAF takes place via its structured LEM domain, interactions with other binding partners and emerin self-association[18,23] are mediated by the IDR. Emerin can indeed oligomerize via regions of the IDR that serve as LEM binding and self-assembly sites between emerin monomers[18], and, in vitro, emerin self-association into filamentous structures[24] impact binding to lamin A/C and BAF[18]. Post-translational modifications in the IDR and the LEM domain also influence the oligomerization of emerin and

its interactions with binding partners[1,25,26]. In isolated nuclei, phosphorylation of emerin residues Y74 and Y95 are required for lamin A/C recruitment to the LINC complex and nuclear envelope stiffening in response to mechanical loads[27]. Additional post-translational modifications regulate the affinity of the LEM domain to BAF[26] and binding to actin[28]. How emerin organizes at the nuclear envelope and participates in protecting the nucleus against mechanical strains remains unclear.

EDMD often involves frame-shift deletions and nonsense mutations of emerin that effectively ablates expression in cells[29]. Yet, a few sets of point mutations and small deletions, including Δ95-99, Q133H and P183H/T, also cause EDMD despite the localization of these mutated emerin at the nuclear envelope and normal cellular expression levels[19,20,30,31]. These emerin mutants display altered self-association and binding to nucleoskeletal proteins in vitro[1,23] and possible changes in their molecular organizations at the nuclear envelope might explain why they induce EDMD.

Here, we used super-resolution imaging by stochastic optical reconstruction microscopy (STORM) and single particle tracking by photoactivated localization microscopy (sptPALM) to investigate the nanoscale organization of wild-type emerin and emerin mutants at the nuclear envelope in cells. By modulating the mechanical landscape of nuclei using cell micropatterning techniques[32], we also studied how emerin participates in nuclear envelope mechanotransduction processes during stress. We show that emerin oligomerization and its differential interactions with key structural partners at the nuclear envelope is central to nuclear shape adaptation against mechanical challenges.

Results

Emerin displays distinct diffusive behaviors at the nuclear envelope

To study the nuclear envelope dynamics of wild-type and dystrophy causing mutations of emerin, PA-TagRFP-emerin fusions were expressed in emerin-null human dermal fibroblasts (HDF) from an EDMD patient ($EMD^{-/y}$)[33]. PA-TagRFP-emerin expression led to the expected localization of emerin at the nuclear envelope, as observed for endogenous emerin in HDF from a healthy individual ($EMD^{+/y}$) (Figure 1a). Upon re-expression of wild-type emerin fusions in $EMD^{-/y}$ HDF, nuclear deformations against mechanical stress also recovered to levels similar to

those of normal *EMD*$^{+/y}$ HDF[34]. For single molecule tracking by sptPALM, individual PA-TagRFP-emerin were imaged using highly inclined and laminated optical sheet (HILO)[35] excitation at the bottom nuclear envelope. Diffusion tracks were generated from localized emerin appearances (Figure 1b and Supplementary Movie 1) and diffusion analyses were performed using the probability distribution of square displacement (PDSD)[36] to separate unique diffusive behaviors (Figure 1c).

From the PDSD analysis of thousands PA-TagRFP-emerin trajectories, we observed that wild-type emerin exhibits four distinct diffusive behaviors with diffusion values D_1: $2.21 \times 10^{-1} \pm 4.9 \times 10^{-2}$ $\mu m^2 s^{-1}$, a value similar to that previously reported for diffusion at the ER membrane[37], D_2: $1.48 \times 10^{-2} \pm 1.5 \times 10^{-3}$ $\mu m^2 s^{-1}$, D_3: $1.73 \times 10^{-3} \pm 1.1 \times 10^{-4}$ $\mu m^2 s^{-1}$, and D_4: $2.6 \times 10^{-4} \pm 1 \times 10^{-5}$ $\mu m^2 s^{-1}$ (Figure 1d and Supplementary Table 1). The putative ER population D_1 makes up 1% of the detected behaviors under HILO imaging, while the next slower population D_2 represents 9%, a small fraction of emerin similar to that expected at the outer nuclear membrane (ONM)[2,6]. The two slowest populations D_3 and D_4 collectively represent 90% of emerin diffusive behaviors. Based on their individual mean square diffusion coefficient, we also grouped emerin trajectories into four diffusion ranges spanning the D values measured from PDSD analyses and plotted them as maps. In trajectory maps, the fastest emerin population D_1 primarily distributes in the immediate proximity of nuclear envelope, a location consistent with diffusion in the ER membrane, while the three slower populations D_2, D_3 and D_4 display enrichment at the nuclear membrane (Figure 1e). Compared to diffusion analyses by fluorescence recovery after photobleaching, where we could detect only two diffusive behaviors of wild-type emerin (Supplementary Figure 1), these measurements show that the mobility of emerin involves four very different types of diffusions at and around the nuclear envelope.

Emerin organizes as slowly diffusing monomers or oligomers at the inner nuclear membrane

Emerin primarily localizes at the INM but a small fraction is often detected at the ONM[2,6], where it does not interact with the nuclear lamina. To further assess if diffusing population D_2 corresponds to emerin specifically associated with the ONM, sptPALM was done after lamin A/C depletion by siRNA (Supplementary Figures 2 and 3). We found that downregulation of lamin A/C expression does not affect the diffusion of emerin populations D_1 and D_2 (*p* not

significant, Figure 2a) but induces increased mobility for D_3 and D_4 ($p<0.01$, Figure 2a and Supplementary Table 1). This shows that emerin with diffusion D_3 (40%) and D_4 (50%) are localized at the INM, while population D_2 (9%) diffuses at the ONM. When nuclear actin is depleted by downregulating the expression of the actin nuclear import factor, importin-9[38] (IPO9, Supplementary Figures 2, 3), a similar increase in the mobility of populations D_3 and D_4 is observed (Figure 2a, and Supplementary Table 1), further indicating that the majority of emerin is distributed as two distinct INM pools, both interacting with the nucleoskeleton.

Emerin can also self-assemble in vitro[23,24] and its potential oligomerization at the INM could result in a slow mobility, in particular if emerin oligomers are tethered by the nucleoskeleton. To determine if diffusing populations D_3 or D_4 correspond to emerin monomers or oligomers, we tracked individual emerin in their dimeric and oligomeric forms. We co-expressed wild-type emerin fusions to self-complementary split-GFP fragments[39] (sGFP-emerin and M3-emerin, Figure 2b) to irreversibly induce the formation of complemented emerin-GFP-emerin species and we studied their lateral mobility by complementation activated light microscopy[40] (CALM). We found that emerin-GFP-emerin species localize almost exclusively at the nuclear envelope (Figure 2c and Supplementary Movie 2), where they diffuse as two separate populations: a dominant 90% population with a mobility similar to D_4 (p not significant, Figure 2d), and a minor 10% population with a mobility similar to the ONM population D_2 (p not significant, Figure 2d). No fluorescent species with diffusion matching those of the ER population D_1 or the INM population D_3 are detected. Emerin-GFP-emerin trajectories often spatially overlap, indicating that emerin forms multimers rather than strictly dimers at the INM (Figure 2c). These data show that population D_3 detected by sptPALM but not by CALM represents emerin monomers, while the slowest population D_4 represents dimers or, more likely, larger emerin oligomers at the INM, as subsequently confirmed by super-resolution imaging. The nearly 10-fold difference in translational diffusion coefficient between populations D_3 and D_4 is close to the 10-40 fold reduction in mobility reported when monomeric membrane proteins transition to oligomers[41]. The detection of a few emerin-GFP-emerin species at the ONM is likely due to split-GFP-induced emerin dimers that cannot translocate through peripheral nuclear pore channels[9] and do not access the INM.

BAF binding modulates the mobility of both emerin monomers and oligomers distributed across the inner nuclear membrane.

BAF binds the LEM domain of emerin with high affinity[18] and, because it also binds lamin A/C[42] and chromatin[43], it likely participates in the slow mobility of emerin at the INM[44]. To study how binding of emerin to BAF might influence its diffusion, endogenous BAF was depleted by siRNA (Supplementary Figures 2 and 3) and replaced by the expression of BAF L58R, a mutant that does not bind the LEM domain of emerin[45]. When unable to bind BAF L58R, emerin monomers diffuse significantly faster with a lateral mobility higher than for lamin A/C or IPO9 knock down ($p<0.01$, Figure 2a and Supplementary Table 1). Emerin oligomers also diffuse faster ($p<0.01$, Figure 2a), indicating that BAF modulates the dynamics of emerin when it oligomerizes at the INM. While emerin diffusion at the ER is undisturbed, its mobility at the ONM increases ($p<0.01$, Figure 2a), suggesting that cytoplasmic BAF also interacts with emerin at the ONM. BAF being highly mobile in the nucleus[44], the comparatively slow mobility of BAF-bound emerin at the INM likely stems from the formation of ternary complexes with lamin A/C or chromatin. Indeed, knock down of endogenous BAF and expression of BAF L58R did not significantly affect the expression levels of lamin A/C nor its nuclear localization (Supplementary Figures 2 and 3). As such, the stronger influence of BAF L58R on emerin dynamics as compared to lamin A/C depletion indicates that BAF binding modulates the mobility of emerin not only via ternary binding to lamin A/C, but also via ternary interactions with other nuclear components, potentially chromatin.

We additionally built diffusion maps of wild-type PA-tagRFP-emerin at the nuclear envelope by spatial rendering of diffusion coefficients at the position of each tracked molecule (Figure 2e). Those maps are dominated by the two slowest INM emerin populations, which represent 90% of the total pool detected. They show that domains with very slow diffusion and attributed to emerin oligomers are distributed throughout the nuclear envelope and are surrounded by diffusion areas where the mobility of emerin is faster and matches that of monomers (Figure 2e). This indicates a membrane-wide, yet locally structured distribution of emerin at the INM, with monomers surrounding emerin oligomer domains in an organization compatible with emerin monomer/oligomer exchanges in distinct INM areas.

Together, these results show that emerin diffuses rapidly at the ER membrane on its way to the juxtaposed ONM, where its diffusion is slower, in part by interaction with cytoplasmic BAF.

Once at the INM, the mobility of emerin is further reduced, with emerin monomers and oligomers interacting with nuclear BAF and the nucleoskeleton. This distribution is consistent with a combined BAF-induced and lamina-induced retention and accumulation of emerin at the INM.

Emerin forms discrete oligomeric nanodomains surrounded by monomers

We then probed the structural organization of emerin in more detail using super-resolution microscopy. Wild-type emerin fused to a SNAP-tag (SNAP-emerin) was expressed in *EMD*$^{-/y}$ HDF and, after chemical fixation, cells were stained with benzylguanine-FluorAlexa647 to image individual emerin by dSTORM (Figure 3a). Emerin neighborhood density functions (NDF) built from localized emerin positions across multiple nuclei were compared to MonteCarlo simulations of completely random distributions and fitted with exponential decay models[46] to measure molecular densities and length scales of significant clustering. We found that wild-type emerin is not distributed randomly at the nuclear envelope, as it displays density distributions significantly higher than expected for a completely random organization (Figure 3b). The NDF is best fitted with a two exponential decay model, indicating that emerin organizes into two distinct clustering states across the nuclear envelope. The first type of cluster is small with a typical cluster size of 22±11 nm and a molecular density of emerin 8.2±0.2 fold higher than expected for a random distribution (Figure 3c and Supplementary Table 2). The second type of cluster is significantly larger with a typical cluster size of 236±30 nm and an emerin density slightly above the expected value of 1 for complete randomness (1.3±0.1 fold, Figure 3c). In cluster maps built from local cluster analyses[47], wild-type emerin forms small high-density clusters scattered throughout the nuclear envelope and surrounded by larger emerin areas with densities close to random (Figure 3d). Those distributions are strikingly similar to sptPALM diffusion maps in live cells (Figure 2e) and corroborate that, across the INM, emerin organizes into small and discrete oligomers surrounded by dispersed emerin monomers. While it is intriguing that emerin monomers appear slightly clustered, a fully random distribution is not to be expected because they do not populate membrane-less areas of the nuclear envelope, such as nuclear pores.

Emerin oligomers are stabilized by lamin A/C and SUN1 and modulated by nuclear actin and BAF

We then determined how lamin A/C, nuclear actin, BAF and SUN1 from the LINC complex participate in the nanoscale spatial organization of emerin at the INM. Wild-type emerin was imaged by super-resolution microscopy after siRNA knock down of lamin A/C, IPO9, SUN1, or replacement of endogenous BAF with BAF L58R. After lamin A/C depletion, the molecular density of emerin is reduced at all length scales (Figure 3b) and emerin distributes into small, 35±17 nm nanodomains with molecular density close to random (1.2±0.1 fold, Figure 3c and Supplementary Table 2) and into larger 950±173 nm emerin monomer domains with density just above random (1.1±0.1 fold, Figure 3c). Compared to distributions in cells having endogenous lamin A/C levels, emerin monomers are dispersed over larger areas and, importantly, emerin oligomers nearly vanish. Such changes in organization are also seen in emerin cluster maps of lamin A/C depleted nuclei, where most oligomeric nanodomains have dissipated, and where monomers cover a significantly larger part of the nuclear envelope (Figure 3e). We note that while lamin A/C depletion indirectly leads to decreased levels of nuclear actin (Supplementary Figures 2), emerin oligomers are not as severely disrupted when nuclear actin is specifically depleted by IPO9 knock down, as shown next. This indicates that lamin A/C plays a central and direct structural role for the stabilization of emerin oligomers and additionally influences the spatial distribution of emerin monomers at the INM.

When nuclear actin is depleted after IPO9 depletion, wild-type emerin forms oligomers having a reduced molecular density of 3.6±0.1 fold above random and a larger size of 65±13 nm compared to untreated cells or cell treated with control siRNA (Figure 3c and Supplementary Table 2). Emerin monomers are dispersed over membrane domains with typical length scales of 382±81 nm, larger than in untreated cells (236±30 nm, Figure 3c), but not as large as for lamin A/C depletion (950±173 nm, Figure 3c). Thus, despite reduced nuclear actin levels, emerin retains the ability to oligomerize, although it disperses over large INM areas. These data show that, together with lamin A/C, nuclear actin contributes to maintaining the overall spatial distribution of emerin at the INM and participates in the structural maintenance of emerin oligomers, albeit to a lesser degree than the lamina itself.

When endogenous BAF is replaced by BAF L58R, wild-type emerin oligomers are still formed but they have a reduced molecular density of 2.0±0.1 fold above random and a larger size of

85±19 nm compared to cells expressing wild-type BAF (Figure 3c and Supplementary Table 2). The inability to bind BAF also induces a re-distribution of emerin monomers over large INM domains with typical sizes of 718±250 nm (Figure 3c). Consistent with our diffusion results, emerin binding to BAF modulates the organization of both oligomeric and monomeric emerin and strongly influences the spatial distribution of emerin monomers at the INM.

When SUN1 is depleted to destabilize LINC complexes (Supplementary Figures 2 and 3), the formation of emerin oligomers is reduced to levels equivalent to those of lamin A/C depletion. Emerin distributes randomly over 75±41 nm nanodomains with molecular densities of 1.2±0.1 fold above random, an extensive decrease compared to oligomeric clusters in cells with endogenous SUN1 expression levels (Figure 3c and Supplementary Table 2). Emerin also distributes at random over nuclear envelope domains with typical sizes of 268±110 nm, similar to the spatial distribution of emerin monomers in untreated cells (Figure 3c and Supplementary Table 2). This indicates that reduced SUN1 expression levels primarily influence the formation of emerin oligomers at the INM. In cluster maps, destabilization of SUN1 LINC complexes effectively results in a largely random distribution of emerin at the INM and, like for lamin A/C depletion, few emerin clusters are visible (Figure 3f). While SUN1 interacts with lamin A[22,48-50], the expression and nuclear envelope localization of lamin A/C was not disrupted by SUN1 knockdown (Supplementary Figures 2 and 3) and, reciprocally, lamin A/C depletion did not modify the expression of SUN1 nor its distribution at the nuclear membrane (Supplementary Figures 2 and 3), as often reported [48,49,51,52]. Thus, together with lamin A/C, SUN1 is required for the stabilization of emerin oligomers and their localized distribution at the INM. SUN1, itself, was shown to self-assemble into nearly immobile oligomeric platforms[53,54] that could potentially serve as sites for macromolecular assemblies at the INM. The observation that a core LINC component, such as SUN1, is required for the self-assembly of emerin at the INM indicates that emerin locally oligomerizes at LINC complexes.

Together, these results show that wild-type emerin monomers are distributed throughout the INM where their dispersion is modulated by direct binding to BAF and additional spatial constrains imposed by lamin A/C and nuclear actin. Emerin also assembles into discrete and small oligomeric nanodomains that are structurally co-stabilized by lamin A/C and the LINC complex protein SUN1 and are maintained, to a lesser extent, by BAF and nuclear actin.

Increased diffusion and oligomerization of emerin upon nuclear adaptation to mechanical stress

We then sought to define the mechanotransducing functions of emerin by studying how its mobility and its nanoscale organization change when nuclei are subjected to increasing mechanical stress. SptPALM and super-resolution imaging of wild-type emerin were done in *EMD*$^{-/y}$ HDF grown on increasingly narrow rectangular micropatterns with widths of 15 µm, 10 µm or 5 µm, to impose steady-state mechanical stress to the nucleus[6,32,34](Figure 4a and 4b) and increase mechanical loads at LINC complexes[55]. First, we verified that changes in nuclear shape index (NSI) on these micropatterns reflect the mechanical adaptation of nuclei against forces by depleting lamin A/C or nuclear actin, two key nucleoskeletal proteins involved in maintaining nuclear shape during stress. In non-patterned cells, nuclei are slightly less circular after lamin A/C or nuclear actin depletion compared to controls ($p<0.01$, Figure 4c). These effects are amplified on micropatterns where nuclei become increasingly deformed as patterns get narrower ($p<0.01$, Figure 4c). This demonstrates that cell micropatterning elicits increased nuclear stress and effectively induces mechanical responses of the nucleus that implicate the nucleoskeleton.

When we tracked wild-type PA-tag-RFP-emerin on deformed nuclei in 15 µm and 10 µm patterns (Supplementary Movie 3), we found that its ER mobility is unchanged compared to non-patterned cells (*p* not significant, Figure 4d and Supplementary Table 1), while its diffusion at the ONM is faster ($p<0.01$, Figure 4d). At the INM, emerin monomers also diffuse significantly faster ($p<0.01$, Figure 4d) and the mobility of oligomers increases compared to non-patterned cells, albeit short of statistical significance for 15 µm patterns (*p* not significant and $p<0.01$, Figure 4d). Interestingly, there is no significant difference in the mobility of all four ER, ONM and INM emerin populations in both types of micropatterns compared to nuclear actin depletion (*p* not significant, Supplementary Figure 4), suggesting that nuclear shape adaptation to mechanical cues entails modified interactions of emerin with nuclear actin, notably for monomers.

Spatial distribution analyses of wild-type SNAP-emerin further indicate that, as the NSI decreases, monomers disperse over increasingly large INM domains with sizes of 382±62 nm and 460±136 nm, compared to 236±30 nm for non-deformed nuclei (Figure 4e). Concurrently, oligomer densities drop from 8.2±0.2 fold to 3.6±0.1 fold above random in 15 µm patterns, before increasing to 4.6±0.1 fold above random in 10 µm patterns (Figure 4e). Remarkably,

oligomeric nanodomains become larger during nuclear stress and their size expands from 22±11 nm to 60±13 nm in both micropatterns (Figure 4e). When considering this wider spatial distribution of oligomers, the relative oligomerization of emerin compared to non-deformed nuclei increases by 3.4 fold and by 4.1 fold as the nucleus adapts to incremental mechanical stress (Figure 4f). This shows that nuclear shape adaptation to forces is associated with a gradual change in the oligomerization potential of emerin at the INM. This enhanced oligomerization of emerin over larger nanodomains is accompanied by a faster lateral mobility of emerin and is triggered by nucleoskeletal re-arrangements. Indeed, the stress-induced spatial reorganizations of emerin in micropatterns, including oligomer densities and emerin domain sizes, are strikingly similar to those observed when nuclear actin is depleted in non-patterned cells (Supplementary Figure 4 and Supplementary Table 2). Consistent with the contribution of nuclear actin to changes in nuclear volume[56], these observations suggest that nuclear shape deformation entails a disengagement of nuclear actin from the nucleoskeleton that results in faster diffusion of emerin monomers and increased oligomerization. An increased lateral mobility of emerin at the INM could indeed facilitate molecular collisions between monomers and the formation of oligomers stabilized by lamin A/C and SUN1 at LINC complexes. These results indicate that the mechanotransducing functions of emerin are coupled to changes in its oligomeric state along the INM and are modulated by emerin interactions with nucleoskeletal partners, including nuclear actin, to ensure appropriate nuclear deformation and response to mechanical challenges.

Emerin mutants induce abnormal nuclear deformation against mechanical stress

To further establish the significance of emerin oligomerization at the INM and its importance for nuclear adaptation to mechanical stress, we then compared the organization of wild-type emerin with that of mutated forms of emerin known to induce EDMD. We studied how emerin mutation Q133H, deletion Δ95-99, and mutation P183H (Figure 5a) affect the lateral diffusion and the nanoscale distribution of emerin at the nuclear envelope. First, we verified that these mutated emerin effectively induce defective mechanical responses of nuclei when expressed in *EMD*$^{-/y}$ HDF by comparing changes in NSI after random cell plating or plating on increasingly narrow rectangular micropatterns (Figure 5b, c). In randomly plated cells, the expression of mutated emerin results in nuclei that are slightly less circular compared to wild-type emerin (Figure 5b). With increasing mechanical stress in micropatterns, cells expressing emerin mutants display

significantly higher NSI values than wild-type (Figure 5b), indicative of a failure to correctly modify the shape of the nucleus in response to forces. These deficient changes in nuclear shape are accompanied by a mispositioning of the nucleus relative to the cell major axis, nucleus crumpling, abnormal organization of the actin cytoskeleton and failure of cells to properly fit within micropatterns, specifically in cell areas adjacent to the misshaped nucleus (Figure 5c). It indicates that expression of mutated emerin in *EMD*$^{-/y}$ HDF effectively impedes nuclear adaptation to mechanical stress.

Emerin mutants display defective oligomerization at the inner nuclear membrane

Q133H mutation

Using sptPALM and super-resolution imaging, we then characterized the nuclear envelope dynamics of each mutated emerin and their respective nanoscale organization, starting with Q133H emerin. We found that the lateral mobility of Q133H PA-TagRFP-emerin is similar to that of wild-type emerin at the ER and the ONM (p not significant, Figure 6a and Supplementary Table 1), but that both Q133H monomers and oligomers diffuse significantly faster at the INM ($p<0.01$ and $p<0.05$, Figure 6a). In vitro, the Q133H mutation disrupts emerin binding to actin[57] but does not impede interactions with lamin A/C[31], SUN1[22] or BAF[58]. The increased lateral diffusion of Q133H, only at the INM, therefore indicates that it does not bind nuclear actin. Interestingly, the faster INM diffusion of Q133H also resembles the increased mobility of wild-type emerin when nuclear actin is depleted (Figure 2a), which further underlines that nucleoskeletal actin modulates the diffusion of emerin monomers and oligomers. This is consistent with previous observations that emerin expression influences the mobility of nuclear actin[59] and indicative of a reciprocal effect of emerin/nuclear actin interactions on their respective mobility. The diffusion of Q133H at the INM is also similar to that of wild-type emerin under mechanical stress, in both 15 µm and 10 µm wide micropatterns (p not significant, Supplementary Figure 5 and Supplementary Table 1), which supports a mechanism where nuclear deformations involve a dissociation of emerin from nuclear actin that leads to faster emerin diffusion at the INM.

Although, it was reported that Q133H has a reduced capacity to self-assemble in vitro[23], our analyses of its spatial distribution and cluster maps show that, like wild-type emerin, it organizes into monomers and oligomers across the INM (Figures 6b and 6c). Q133H monomers are

distributed in 213±62 nm membrane domains, a size similar to that of wild-type emerin (Figure 6b), which indicates that the inability to bind nuclear actin increases the mobility of Q133H monomers but does not affect their overall spatial distribution at the INM. Q133H also retains the ability to self-assemble at the INM where it forms oligomeric clusters having sizes of 19±12 nm, similar to the 22±11 nm size of wild-type emerin oligomers, but with molecular densities 12.2±0.2 fold above random (Figure 6b, c and Supplementary Table 2). This 50% increase in oligomerization compared to wild-type emerin indicates that the deficient binding of Q133H to nucleoskeletal actin leads to a disproportionate self-association of emerin into oligomeric nanodomains. It also implies that direct binding to nuclear actin normally reduces the oligomerization potential of wild-type emerin.

Δ95-99 mutation

When we performed similar studies with Δ95-99 emerin, we found that its diffusion at the ER membrane and the ONM is unchanged compared to wild-type emerin (*p* not significant, Figure 6d and Supplementary Table 1), but that its lateral mobility at the INM is significantly reduced ($p<0.05$ and $p<0.01$, Figure 6d). This suggests that Δ95-99 interacts more strongly or more frequently than wild-type emerin with some of its binding partners on the nucleoplasmic side of the nuclear envelope. Previous biochemical studies have shown that the small Δ95-99 deletion eliminates emerin interactions with most of its binding partners, including lamin A/C and actin, but not BAF[1]. As we observed, BAF binding strongly influences the mobility of wild-type emerin (Figure 2a) and the reduced diffusion of Δ95-99 at the INM could stem from repetitive interactions with BAF, as recently proposed[24]. To destabilize these interactions, we attempted to track Δ95-99 in *EMD*$^{-/y}$ HDF knocked down for endogenous BAF and expressing BAF L58R. Co-expression of both Δ95-99 and BAF mutants, however, proved toxic to cells, indicating that interactions between Δ95-99 emerin and BAF are important to maintain cell viability.

In addition to the slow mobility of emerin at the INM, the Δ95-99 deletion induces defective oligomerization. Δ95-99 is distributed randomly over large, 420±51 nm nuclear envelope domains and in smaller, 48±14 nm nanodomains where the molecular density of 1.3±0.1 fold above random is largely reduced compared to wild-type emerin oligomers (Figure 6e and Supplementary Table 2). Effectively, Δ95-99 forms less dense and fewer oligomerization nanodomains in cluster maps (Figure 6f). Thus, Δ95-99 does not efficiently oligomerize at the

INM, consistent with its impaired self-assembly in vitro and observations that the deletion lowers emerin/emerin proximity[23]. Interestingly, despite an intact lamina and the preserved ability of Δ95-99 to bind SUN1[22], the molecular densities and cluster maps of Δ95-99 are similar to those of wild-type emerin when the expression of lamin A/C is reduced or when SUN1 LlNC complexes are disrupted (Figure 3c, d). This decreased oligomerization of Δ95-99 to levels seen after lamin A/C depletion implies that direct binding to lamin A/C is required to stabilize emerin oligomers at SUN1 LINC complexes. Such a stabilizing role of lamin A/C is consistent with prior proximity ligation assays where Δ95-99 was found less close to lamin A/C than wild-type emerin[23] and in vitro studies showing that the deletion abolishes direct lamin A/C binding to emerin[20]. Together, these results show that Δ95-99 fails at oligomerizing and primarily distributes at random throughout the INM due to its reduced self-association, its inability to directly bind lamin A/C and its slow mobility.

P183H mutation

Like for the two other emerin mutants, sptPALM tracking of P183H emerin reveals that its lateral diffusion at the ER membrane and the ONM is unchanged compared to wild-type emerin (p not significant, Figure 6g and Supplementary Table 1). However, its mobility at the INM is reduced for the populations attributed to monomers and oligomers ($p<0.05$ and $p<0.01$, Figure 6g). This slow diffusion is similar to that observed for Δ95-99 and again implies that P183H interacts more frequently than wild-type emerin with some of its nucleoplasmic binding partners. In vitro, P183H maintains its binding to many emerin partners, including SUN1[22], BAF and actin[1] and displays enhanced binding to lamin A/C compared to wild-type emerin[1,20]. The observed reduced INM diffusion of P183H might therefore be linked to an increased binding frequency to BAF, like for Δ95-99, or to its enhanced binding to lamin A/C. However, the slow INM mobility of P183H could also be due to the formation of dimers as recently suggested based on its the strong propensity to self-assemble in vitro[23] and observations that residue P183 is positioned in the 168-186 emerin region required to limit emerin-emerin association[18]. To determine if P183H tends to form dimers at the nuclear envelope, we performed single particle tracking by CALM after co-expression of sGFP-P183H and M3-P183H emerin. Three different populations of fluorescently activated P183H-GFP-P183H emerin species were detected at the nuclear envelope: a 2% population with a mobility slightly slower than P183H at the ER

membrane ($p<0.05$, Figure 6g), a larger 39% population with a mobility comparable to the ONM behavior of P183H (*p* not significant, Figure 6g), and a dominant 59% population with a lateral diffusion similar to the INM population initially attributed to P183H monomers by sptPALM (*p* not significant, Figure 6g and Supplementary Table 1). Surprisingly, no fluorescent species with diffusion coefficient matching that of the slowest P183H oligomers are detected (Figure 6g). The high frequency detection of complemented split-GFP at both the ER membrane and the ONM indicates that P183H is more prone to self-assemble and to form dimers than wild-type emerin before reaching the INM. This apparent biased monomer:dimer equilibrium towards dimers is maintained at the INM where it precludes an efficient association of P183H into oligomer domains, in particular when dimers are further stabilized by irreversible assembly of the split-GFP fragments. This shows that P183H has a strong propensity to form dimers that could impact oligomerization at the INM.

Consistent with these observations, spatial analyses reveal that the dimerization of P183H leads to a significantly reduced oligomerization at the INM. P183H monomers/dimers are distributed in domains with typical sizes of 321±29 nm and molecular densities of 1.3±0.1 fold above random (Figure 6h and Supplementary Table 2). Smaller, 35±12 nm nanodomains are also observed, but their molecular density is reduced to 2.2±0.1 compared to wild-type emerin oligomers (Figure 6h). Indeed, while P183H can still bind lamin A/C and SUN1, it forms oligomeric domains having lower molecular density than wild-type emerin in cluster maps (Figure 6j) indicating that the dimerization of P183H hinders further self-association into dense oligomers at the INM.

Abnormal reorganization of Δ95-99 emerin in response to mechanical stress

In order to characterize the importance of emerin oligomerization for nuclear deformation and responses to mechanical stress, we also studied the nanoscale organization of Δ95-99 in micropatterned cells. For deformed nuclei in 15 µm patterns, Δ95-99 monomers are dispersed over large, 810±215 nm INM domains, almost double the size of monomer domains in non-stressed nuclei (420±51 nm, Figure 7a). However, as abnormal nuclear deformations become more pronounced in 10 µm patterns, the distribution of Δ95-99 monomers return to non-stress levels, with dispersions in domains 499±250 nm in size (Figure 7a). Thus, contrary to wild-type emerin, a progressive dispersion of Δ95-99 monomers over increasingly large INM areas is not

observed with growing mechanical stress, consistent with the abnormal changes in NSI induced by the deletion (Figure 5b). At the same time, the formation of emerin oligomers remains very limited, with Δ95-99 molecular densities increasing slightly from 1.3±0.1 to 1.7±0.1 and 2.0±0.1 fold above random in 15 µm and 10 µm micropatterns (Figure 7a and Supplementary Table 2). With the concurrent size enlargement of nanodomains from 48±14 nm to 81±16 nm and 75±20 nm, the relative oligomerization of Δ95-99 compared to non-mechanically stressed nuclei increases by 3.9 fold initially, but does not rise further as nuclear stress intensifies (Figure 7b). Δ95-99 oligomeric nanodomains remains sparser and significantly less dense than for wild-type emerin in cluster maps of nuclei under stress (Figure 7c). Thus, compared to wild-type emerin, the failure of Δ95-99 to gradually self-associate at sufficiently high molecular densities leads to defective nuclear responses to force. This underlines the importance of modulating the oligomerization of emerin as a function of mechanical stress intensity for adaptive nuclear deformations.

Discussion

Using a combination of single molecule imaging and quantitative measurements, we showed that emerin is distributed as monomers and oligomers at the INM and that clinically relevant EDMD mutations induce modified emerin mobility and nanoscale organizations. The oligomerization of emerin at specific sites across the nuclear envelope is modulated by its ability to engage or disengage interactions with different structural elements juxtaposed to the INM, including lamin A/C, SUN1, nuclear actin and BAF. Lamin A/C and SUN1 LINC complexes are both essential for a stabilization of emerin oligomers and balanced interactions of emerin with BAF and nuclear actin further modulate its diffusion and its oligomerization potential. We also showed that the mechanotransducing functions of emerin are coupled to its oligomeric state, with the formation, stabilization and maintenance of emerin oligomers being central to nuclear shape adaptation against forces. Indeed, EDMD-inducing mutations that affect emerin oligomerization and its binding to structural elements at the INM lead to abnormal nuclear deformation and defective nuclear positioning in response to mechanical stress.

While the altered in vitro binding properties of Q133H, Δ95-99 and P183H emerin mutants result in expected differences in organization in vivo, they do not necessarily induce fully predicable changes in diffusion and distribution at the nuclear envelope. In effect, via its flexible IDR,

emerin appears to mediate complex interactions with itself, lamin A/C, SUN1, nuclear actin and BAF, where binding to one partner impacts oligomerization and, interdependently, affects interactions with other partners. As shown from the organization of wild-type emerin after nuclear actin depletion and our study of the Q133H emerin mutant, binding to nuclear actin significantly influences the mobility and the oligomerization potential of emerin. Compared to emerin, actin is relatively large and its binding to the IDR of emerin could mask interaction domains that normally serve as LEM binding and self-association sites between emerin monomers[18]. IDR masking, combined with the reduced lateral mobility of actin-bound emerin, might therefore modulate the formation of oligomers by limiting molecular collisions between emerin monomers. Consistent with the need to precisely adjust the oligomerization potential of emerin for adaptive nuclear shape deformations, increased emerin diffusion and controlled formation of emerin oligomers are coupled molecular events during nuclear adaptation against stress, as shown by our measurements in micropatterns. We thus speculate that the deficient binding of Q133H emerin to nuclear actin and its over-oligomerization at SUN1 LINC complexes are linked to the abnormal nuclear deformation observed in cells expressing this mutant.

The differential interactions of emerin with its nucleoplasmic partners and their influence on its mobility and its oligomerization are also underlined by the surprisingly slow lateral diffusion of the Δ95-99 emerin mutant, which does not bind lamin A/C nor actin in vitro, but retains binding to BAF. The 48-118 region of emerin, where Δ95-99 is located, was suggested to act as a potential binding site for the LEM domain[18] and through altered region flexibility, the deletion might reduce the efficacy of such interactions, potentially causing the LEM domain to bind BAF more frequently [24]. Such repeated interactions of Δ95-99 with BAF and, indirectly, with the lamina or chromatin via ternary BAF complexes, could slow its diffusion, limit molecular collisions, and, as our data show, impede its oligomerization by sequestering the LEM domain and reducing bridging interactions with LEM binding sites on other emerin. The Δ95-99 deletion, within the 55-132 lamin tail-binding region of emerin[18], could also prevent a stabilization of already sparse Δ95-99 oligomers by direct lamin A/C binding, as we observed. In the light of these observations, we postulate that the aberrant nuclear deformation against stress of cells expressing Δ95-99 emerin stem from out of balance interactions of the deletion mutant with BAF and its inability to form lamin A/C-stabilized oligomers at SUN1 LINC complexes.

A similar impediment of *in trans* interactions between the LEM domain and self-association sites along the joined IDR of P183H dimers likely result in the reduced ability of this emerin mutant to oligomerize, despite its retained binding to lamin A/C and SUN1. The reported enhanced binding of lamin A/C to P183H emerin[1,20], in close proximity to these same self-association sites could also interfere with inter-emerin bridging interactions. In both cases, the inability of the LEM domain to access binding sites along the IDR would elicit its repeated interactions with BAF, leading to the observed slow diffusion of P183H at the INM. The defective nuclear shape adaptation to mechanical challenges of cells expressing P183H might therefore arise from emerin dimerization and excessive interactions with BAF or lamin A/C that prevent an efficient formation of emerin oligomers at LINC complexes.

As we have shown, because Δ95-99 emerin does not self-assemble into sufficiently dense oligomers at the INM, it induces aberrant nuclear shape remodeling against mechanical stress. The phosphorylation of emerin residues Tyr 74 and Tyr 95 by Scr kinase[60] was previously shown to mediate the recruitment of lamin A/C to the LINC complex during nuclear stiffening in response to force[27]. Our findings that Δ95-99 fails at promoting adaptive nuclear deformation in response to mechanical cues by its reduced ability to form lamin A/C- and SUN1-stabilized emerin oligomers is consistent with the major role played by Tyr 95 phosphorylation for emerin-mediated mechanotransduction at the nuclear envelope. The abnormal organization of cytoskeletal actin we observed in mechanically challenged cells expressing Δ95-99, akin to disorganizations detected with a non-phosphorylable tyrosine 74-95FF emerin mutant[27], also suggests that emerin oligomers are required to strengthen the connection between lamin A/C, the LINC complex and cytoskeletal filaments in order to promote correct nucleus positioning and deformation. These data point towards a link between Tyr 95 phosphorylation, emerin oligomerization and recruitment of lamin A/C for stiffening the nuclear envelope at LINC complexes, likely driven by phosphorylation-induced changes in emerin conformation and binding to nuclear partners[26,27,60]. It is thus possible that emerin oligomeric nanodomains at the INM are enriched in Tyr 95 phosphorylated emerin, lamin A/C and LINC complex components such as SUN1, while emerin monomers populate the rest of the INM, consistent with emerin enrichments in distinct nucleoskeletal “niches” at the nuclear envelope[26].

Taken together, these lines of evidence support a model in which, during stress responses, transient unbinding of emerin monomers from nuclear actin and BAF favors oligomerization by

increasing the lateral diffusion of emerin at the INM and exposing both its LEM domain and self-association sites along its IDR for intermolecular binding between emerin at LINC complexes (Fig. 8). Within emerin oligomers, stabilization by direct interactions with lamin A/C and SUN1 and additional modulation of emerin self-association by nuclear actin and BAF likely allow for a precise regulation of the oligomerization potential and the size of emerin oligomeric nanodomains at LINC complexes as required for adaptive nuclear deformation in response to forces. The localized INM distribution of emerin oligomers, the involvement of lamin A/C in their stabilization, their specific disruption following SUN1 depletion and their reliance on a part of the emerin IDR that requires phosphorylation for the recruitment of lamin A/C to the LINC complex[27], indeed support the idea that they are sites where interactions between emerin, lamin A/C and LINC components are strengthened. Along similar lines, it was recently suggested that the clustering of SUN proteins might enable them to sustain high forces at the nuclear envelope during force-dependent processes[61]. Emerin oligomerization at SUN1 LINC complexes, might therefore contribute to the increased connectivity between the nucleoskeleton, the nuclear envelope and the cytoskeleton for anchoring the nucleus and providing force absorption contact points during nuclear deformation.

In response to surging mechanical stress, the incremental oligomerization of emerin in enlarged nanodomains we observed could be part of a mechanism that redistributes increasing forces over wider areas at LINC complexes to maintain a basal membrane pressure at these anchoring points between the nucleoskeleton, the nuclear envelope and the cytoskeleton. Beyond this central role played by emerin oligomers, our data point to additional emerin functions outside these anchoring oligomeric nanodomains. For instance, the disengagement of emerin monomers from nuclear actin likely reduces nuclear envelope contacts with the nucleoskeleton, while some membrane connectivity with nuclear chromatin is maintained, via BAF. Indeed, both nucleoskeleton and chromatin tethering to the nuclear envelope participate in nuclear mechanics[5,62]. Together, strengthening the connections between the nuclear envelope, the lamina and the cytoskeleton at SUN1 LINC complexes, but partially relaxing them in the rest of the membrane could provide a means to couple controlled nuclear deformation with nucleus positioning in cells. As we have shown, such coupling is defective with emerin mutants, which display modified interactions with nucleoplasmic partners and abnormal oligomerization.

Additional cross-correlative studies will be needed to further define how the structural interdependencies between emerin monomers, emerin oligomers, SUN1, BAF, and key elements of the nucleoskeleton spatially regulate INM/lamina and INM/chromatin contacts and reinforce the connections between the nuclear envelope and the cytoskeleton at LINC complexes during nuclear responses to force. At the center of these processes, emerin diffusion and monomer/oligomer exchanges provide a means to transduced mechanical cues throughout the entire nuclear envelope, for coordinated changes in local nuclear stiffness and remodeling of the nuclear shape.

Materials and Methods

Cell culture, emerin expression and cell staining

Emerin-null human dermal fibroblast (*EMD*$^{-/y}$ HDF) and normal dermal fibroblasts (*EMD*$^{+/y}$ HDF) were kindly provided by Dr. Howard Worman, Columbia University, New York, USA. *EMD*$^{-/y}$ HDF are derived from a male EDMD patient (G-9054) and carry a 59 nucleotide deletion within the *EMD* gene (*EMD* g.329del59) that ablates emerin expression[22]. HDF were grown in DMEM (Lonza) with 10% fetal bovine serum (Gibco-Life Technologies), 50 units ml^{-1} penicillin and 50 μg ml^{-1} streptomycin and maintained at 37°C in a humidified atmosphere with 5% CO_2.

Human wild-type emerin cDNA was kindly provided by Dr. Juliet Ellis, University College London, UK. For the expression of PA-TagRFP-emerin, a pEGFP-N1 plasmid backbone encoding emerin fused to the C-terminus of PA-TagRFP was produced by XbaI and KpnI insertion and PCR fusion of the human emerin cDNA. Cells plated on fibronectin-coated glass coverslips were transfected with PA-TagRFP-emerin using X-tremeGENE HP (Roche). 48-72 hours post-transfection, live cells were imaged by sptPALM in HBSS buffer at 37°C. For micropatterning experiments, cells grown on 6-well plates were trypsinized after 48-72 hours of transfection and plated on fibronectin-micropatterned coverslips.

To express SNAP-emerin, human emerin was first fused to the C-terminus of a SNAP tag by AscI and XhoI insertion in a pSNAP-tag(m) plasmid (NEB). SNAP-emerin was then subcloned into a modified pFUW lentiviral vector by NheI and AgeI insertion. Lentiviral particles for the expression SNAP-emerin were produced by the UCLA Vector Core. Transduction of HDF grown at 70% confluence on 6-well plates was done for 48 hours, using 25 ng ml^{-1} of lentiviral

particles in complete growth medium containing 8 μg ml^{-1} of polybrene, after which the medium was replaced. Following another 24 hours incubation, cells were trypsinized, and plated on fibronectin-coated or fibronectin-micropatterned coverslips. For imaging, cells were fixed with 4% paraformaldehyde in PBS for 15 min, permeabilized with 0.1% Triton X-100 (Sigma-Aldrich) for 15 min and blocked with 4% bovine serum albumin (BSA, Sigma-Aldrich) + 0.1% Tween-20 (Sigma-Aldrich) for 30 min, at room temperature. Cells were then stained with 1 μM of SNAP-Surface-AlexaFluor 647 (BG-A647, NEB) in 4% BSA + 0.1% Tween-20 for 1 hour at 37°C, then thoroughly washed before super-resolution imaging.

For the expression of sGFP-emerin, humanized cDNA for split-GFP 1-10[40] was inserted by NheI and XbaI digestion in the pEGFP-N1 plasmid backbone encoding emerin, and expressed as an N-terminal fusion to emerin. The shorter 11th β-sheet M3 fragment[40] was also fused to the N-terminus of emerin by PCR cloning using primers encoding the M3 fragment sequence and subcloning into the pEGFP-N1 backbone via NheI and XhoI digestions. Both plasmids were co-transfected in HDF using X-tremeGENE HP (Roche) as described for PA-TagRFP-emerin, and cells were imaged by CALM 48-72 hours post-transfection. All constructs were verified by sequencing.

For immunostaining of emerin, cells were grown on coverslips, fixed and permeabilized as described for SNAP-emerin staining. Cells were labeled with a rabbit anti-emerin antibody (1:500, Santa Cruz Biotechnology, sc-15378) for 45 min, washed in PBS and further labeled with a goat anti-rabbit Alexa fluor 488 antibody (1:400, Invitrogen) for 45 min. After washing, cells were mounted in a DAPI-Fluoromount G (Electron Microscopy Sciences) and imaged by confocal microscopy.

To label cytoplasmic actin and measure nuclear shape indices, cells were fixed with 4% paraformaldehyde in PBS for 15 min, permeabilized with 0.1% Triton X-100 for 10 min, and blocked with 4% bovine serum albumin + 0.1% Tween-20 for 1 hour. Cells were stained with phalloidin-iFluor 488 (1:1000, Abcam) for 1 hour, washed with PBS, mounted in DAPI-Fluoromount G and imaged by confocal or wide field microscopy.

Mutations, siRNA and BAF L58R expression

Emerin mutations Q133H and P183H were introduced in PA-TagRFP-emerin, SNAP-emerin, sGFP-emerin and M3-emerin by site-directed mutagenesis using QuickChange Lightning Site Directed Mutagenesis (Agilent) and mutagenic primer pairs for:

Q133H: 5'-CGCTTTCCATCACCATGTGCATGATGA-3' and
5'-GATCGTCATCATGCACATGGTGATGGA-3'

P183H: 5'-CCTGTCCTATTATCATACTTCCTCCTC-3' and
5'-GTGGAGGAGGAAGTATGATAATAGGA-3'.

The Δ95-99 emerin deletion was produced using partially phosphorothioated PCR primers and T7 exonuclease digestion, as previously described[63]. Primers pairs for the Δ95-99 deletion were:

5'-GACTACTTCACCA*C*C*A*GGACTTAT-3' and
5'-GGTGAAGTAGTCG*T*C*A*TTGTAGCC-3',

where * denotes phosphorothioate modifications. All primers were obtained from Integrated DNA Technologies (IDT) and all mutations were verified by sequencing. siRNA duplex for BAF and Dicer siRNA for lamin A/C, SUN1 and controls were obtained from IDT. The sequences of sense nucleotides were as follows:

- BAF siRNA: 5'-AGAUUGCUAUUGUCGUACUUU-3'
- Lamin A/C DsiRNA: 5'-AGCUGAAAGCGCGCAAUACCAAGaa-3',
- SUN1 DsiRNA 5'- GCUUUUAGUAUCAACCACGUGUCaa-3'.
- Control DsiRNA: 5'-CGUUAAUCGCGUAUAAUACGCGUat-3' (IDT#51-01-14-04).

siRNA duplex for IPO9 was obtained from Ambion (id # S31299). All siRNA were transfected or co-transfected with emerin plasmids at 25 nM using X-tremeGENE HP (Roche). When associated with lentiviral expression of emerin, siRNA transfection was done 2 hours before viral titer application.

BAF L58R was expressed from an EGFP-BAF L58R lentiviral plasmid[45] (Addgene #101776) and lentiviral particles were produced by the UCLA Vector Core. HDF cells were transduced with 25 ng ml^{-1} of lentiviral particles as described for SNAP-emerin.

Cell micropatterning and nuclear shape index measurements

HDF were micropatterned as described previously[32,34]. Briefly, hexamethyldisilazane-activated glass coverslips (Marienfeld, #1.5, Ø25 mm) were stamped with rectangular and fibronectin-coated polydimethylsiloxane stamps having lengths of 210 µm and widths of 15 µm, 10 µm, or 5 µm respectively. Cell attachment outside the fibronectin strips was blocked with a 1% solution of Pluronic F-127. After attachment for 1 hour and removal of unattached cells, HDF were allowed to spread out on the micropatterns for 6 hours at 37°C before being prepared for microscopy imaging.

Using ImageJ[64], the nuclear shape index (NSI)[65] was determined by measuring the nuclear cross-sectional area and the nuclear perimeter of DAPI-stained nuclei imaged by wide-field microscopy, and by calculating the ratio:

$$\mathrm{NSI} = \frac{4 \times \pi \times \mathrm{area}}{\mathrm{perimeter}^2} \qquad (1)$$

The NSI measures the roundness of the nucleus with an NSI of 1 corresponding to a circular nuclear shape. Mean NSI values ± standard deviation of the mean are reported for multiple cell nuclei per condition.

Microscopy imaging

Confocal imaging of immunostained emerin in normal HDF, emerin-null HDF and emerin null HDF after expression of wild-type PA-TagRFP-emerin were performed on an Olympus Fluoview FV1000 confocal microscope equipped with a 60x/1.40 NA objective, 405 nm and 488 nm lasers and appropriate emission filters for imaging DAPI (450/20 nm) and Alexa-488 labeled antibodies against emerin (510/10 nm).

Confocal imaging of nuclear deformation and actin organization in micropatterned *EMD*$^{+/y}$ HDF was performed on a Zeiss LSM 700 microscope equipped with a C-Apochromat 63×/1.15 W Korr objective, excitation lasers at 405 nm and 488 nm and appropriate beamsplitter and emission channel settings for dual detection of DAPI and phalloidin-iFluor 488.

Wide-field imaging of labeled actin and labeled nuclei for NSI measurements were performed on an inverted Nikon Eclipse Ti-E microscope equipped with a 40x objective (Nikon), an iXon Ultra EMCCD camera (Andor), 405 nm and 488 nm lasers, a T495lpxr dichroic mirror and a 525/50 emission filter (Chroma) for phalloidin-iFluor 488 or a 458Di02 dichroic mirror and a 483/32 emission filter (Semrock) for DAPI.

SptPALM, dSTORM and CALM imaging were performed on an inverted Nikon Eclipse Ti-E microscope equipped with a 100x 1.49 NA objective (Nikon), an iXon EMCCD camera (Andor), perfect focus drift compensation optics, an astigmatic lens for 3D super-resolution imaging, a piezo z-scanner for calibration of 3D super-resolution images (Mad City Labs), laser lines at 405, 488, 561 and 647 nm (Agilent), a multiband pass ZET405/488/561/647x excitation filter (Chroma), a quad-band ZT405/488/561/647 dichroic mirror (Chroma) and appropriate emission filters for sptPALM imaging of PA-tagRFP (600/50 nm, Chroma), 3D-dSTORM imaging of Alexa-647 (700/75 nm, Chroma) and CALM imaging of complemented split-GFP (525/50 nm, Semrock).

sptPALM of PA-TagRFP-emerin was performed in 37ºC HBSS buffer (Corning) by HILO excitation of the bottom nuclear membrane of cells with a continuous and low power photoactivation at 405 nm and an excitation at 561 nm. The HILO illumination angle was θ= 51.6º. Images were acquired continuously at a frame rate of 40 ms per frame for no longer than 3 minutes per cell to limit UV damage. CALM imaging of complemented emerin-GFP-emerin species was done as described for sptPALM but with a single HILO excitation at 488 nm.

dSTORM of SNAP-emerin labeled with BG-A647 was performed at room temperature in a photoswitching buffer composed of 10% glucose, 0.5 mg ml^{-1} glucose oxidase (Sigma), 40 µg ml^{-1} catalase (Sigma), and 1% β-mercaptoethanol (Sigma). Continuous photoswitching was achieved with a low power 488 nm laser and imaging was done with a 647 nm laser excitation at a frame rate of 80 ms per frame. Z-calibration and sample drift corrections were done using a few 40 nm TransFluoSphere beads (488/685 nm, Life Technologies) as fiducial markers spread on the cell samples.

Analyses of diffusion coefficients

Localization and tracking analyses were performed using the software package SLIMfast, which uses multiple-target tracing algorithms[66] and was kindly provided by Christian Ritcher and Jacob Piehler. Localizations were performed by 2D-gaussian fitting of the point-spread-function of each activated PA-TagRFP-emerin or activated emerin-GFP-emerin species in each frame. Localization precision was determined as previously described[67], and individual PA-TagRFP-emerin were localized with a precision of 13±5 nm. Diffusion trajectories were built by linking localizations frame to frame and accounting for blinking statistics and local particle densities.

Trajectories with fewer than three steps were discarded. Diffusion coefficients were estimated using a probability density of square displacement (PDSD) analysis[36]. For each time lag *t*, the PDSD curve was fitted with the following model:

$$P(\vec{r}^2, t) = 1 - \sum_{i=1}^{n} a_i(t) e^{-r^2/r_i^2(t)} \qquad (2)$$

$$\sum_{i=1}^{n} a_i(t) = 1$$

where $r_i^2(t)$ is the square displacement and $a_i(t)$ is the population density of *i* numbers of diffusive behaviors at each time lag *t*. To limit the risks of overfitting or underfitting the PDSD curves and select an appropriate model for *i* numbers of diffusive behaviors in each data set, we used both an Akaike information criterion (AIC) and a Bayesian information criterion (BIC) after fitting PDSD with models where $1 \leq i \geq 5$. Square displacement curves ($r_i^2(t)$) were extracted from PDSD analyses and reported with error bars determined using $\frac{r_i^2}{\sqrt{N}}$, where N is the number of analyzed trajectories per time lag, as previously described[36]. Diffusion coefficients (*D*) representative of each behaviors were determined by fitting each $r_i^2(t)$ curves over the first four time lags (t_1-t_4) using OriginPro 2020 software (OriginLab) and a 2D Brownian diffusion model with position error:

$$r^2 = 4Dt + 4\sigma^2 \qquad (3)$$

All diffusion coefficients *D* are reported in $\mu m^2\ s^{-1}$ ± standard error of fit value (± s.e.m.). Statistical comparisons between *D* values were done using F-tests. Population percentages are derived from the averaged $a_i(t)$ values over the considered time lags.

Individual diffusion coefficients (D_i) were obtained by fitting the individual mean square displacement (MSD) for each detected emerin over the first three time lags (t_1-t_3), using again a 2D Brownian diffusion model. Based on their individual D_i value, emerin trajectories were grouped into four diffusion ranges (D_{i1}> 0.1 $\mu m^2\ s^{-1}$, 0.1<D_{i2}> 0.01 $\mu m^2\ s^{-1}$, 0.1<D_{i3}> 0.001 $\mu m^2\ s^{-1}$, and D_{i4}< 0.001 $\mu m^2\ s^{-1}$) and plotted as maps.

Spatial distribution and cluster analyses from super-resolution images

After 3D-dSTORM super-resolution imaging, the localization of individual emerin molecules and z-position assignments were performed by Gaussian fitting using rapidSTORM (version 3.3.1)[68]. Sample drift and overcounting corrections for molecules appearing in consecutive frames were done using PALMsiever[69] and renderings of super-resolved images were done using ImageJ[64]. Localization precisions (σ) in the x, y, and z dimensions were evaluated as previously described[32] and were σ_x:8.3 nm, σ_y:13.0 nm, and σ_z:28.4 nm. 2D spatial pattern analyses of emerin distributions were performed on 2 µm x 2 µm regions of interest (ROI) typically chosen in nuclear envelope areas having homogenous z ranges and away from the edges of nuclei, in order to limit 3D effects.

Emerin clustering was determined using an edge-corrected neighborhood density function (NDF) as previously described[32]. Briefly, the NDF is a pairwise-correlation function similar to O-ring statistics that tallies the density of detected emerin within a ring of outer radius r and width Δr located at a distance r from an emerin position in the ROI and for all $r + \Delta r$ in the ROI. The density of emerin as a function of distance from an average emerin was obtained with:

$$D_r = \frac{\sum N_r}{\sum A_r} \qquad (4)$$

where N_r is the number of neighbors and A_r is the area summed over all detected emerin. NDF analyses were done over a 1µm distance on selected ROIs and with a fixed ring width of 10 nm and a ring radius increasing by 10 nm steps. To average NDF statistics from multiple ROIs across different nuclei and make them sample-size independent, D_r was further standardized by dividing it by the mean density of detected emerin across the entire ROI. As such, an NDF value at a given radius indicates the relative clustering of emerin as compared to the average density across the entire sample. This relative NDF gives a value of 1 for a completely random spatial distribution as determined by Monte Carlo simulations of random emerin distributions with area and number of randomly seeded emerin equal to that of each experimental ROIs.

Relative NDF curves averaged across multiple ROIs and multiple nuclei were fitted with a previously described model[32], which accounts for a distribution of cluster lengths that includes two populations of emerin (monomer and oligomers) and for a probability density of emerin in 2D clusters that decays approximately as an exponential function[46]:

$$\text{Relative NDF} = \{A_1 \times \exp\left(\frac{-r}{\varepsilon_1}\right) + A_2 \times \exp\left(\frac{-r}{\varepsilon_2}\right) + 1\} s * g(r)^{PSF} \quad (5)$$

where, A is the clustering density, ε is the typical half-maximum cluster length, $*$ denotes a 2D convolution, and $g(r)^{PSF}$ is the correlation function of the effective point spread function of uncertainty in position determination for the dSTORM experiments. As described previously[32], $g(r)^{PSF}$ corrects the NDF for contribution of multiple single molecule appearances (blinking) to the overall spatial distribution. After fitting relative NDF curves, the molecular density above random for emerin clusters are reported as A ± standard error of the fit (±s.e.m) and their typical length scales as $2 \times \varepsilon$ ± standard error of the fit and localization precision (±s.e.m). Relative increases in emerin oligomer formation during nuclear stress were determined by considering a circular shape of oligomer nanodomains and multiplying the area of oligomerization by the measured molecular density.

Cluster maps

Cluster maps were generated from drift- and overcounting-corrected super-resolved emerin positions by determining local cluster values around each emerin using the Getis and Franklin L function[47] in spPack[70] and for a distance of 25 nm. Spatial positions in x and y, and cluster values were plotted as maps in MATLAB (MathWorks) using the meshgrid and griddata functions, a 1 nm x 1 nm pixel size and the 'v4' option when calculating pixel density values. The contour maps were generated using the countourf function with 200 levels. In contour maps, values $L(r_{25})=25$ represent areas where emerin is randomly distributed and $L(r_{25})=70$ values represent areas with emerin local density $(70/25)^2$ = ~8-fold higher than expected for a random distribution.

ACKNOWLEDGMENTS

This work was supported by the National Institute of Arthritis and Musculoskeletal and Skin Diseases of the National Institutes of Health under award number R21AR076514. We are grateful to H. Worman for providing emerin null and normal human dermal fibroblasts and to J. Ellis for providing human emerin cDNA.

AUTHOR CONTRIBUTIONS

A.F. and M.B. designed and performed experiments, contributed reagents and analyses, and participated in writing of the manuscript. F.P. conceived and supervised the research, designed and performed experiments, contributed analyses and wrote the manuscript.

COMPETING FINANCIAL INTERESTS

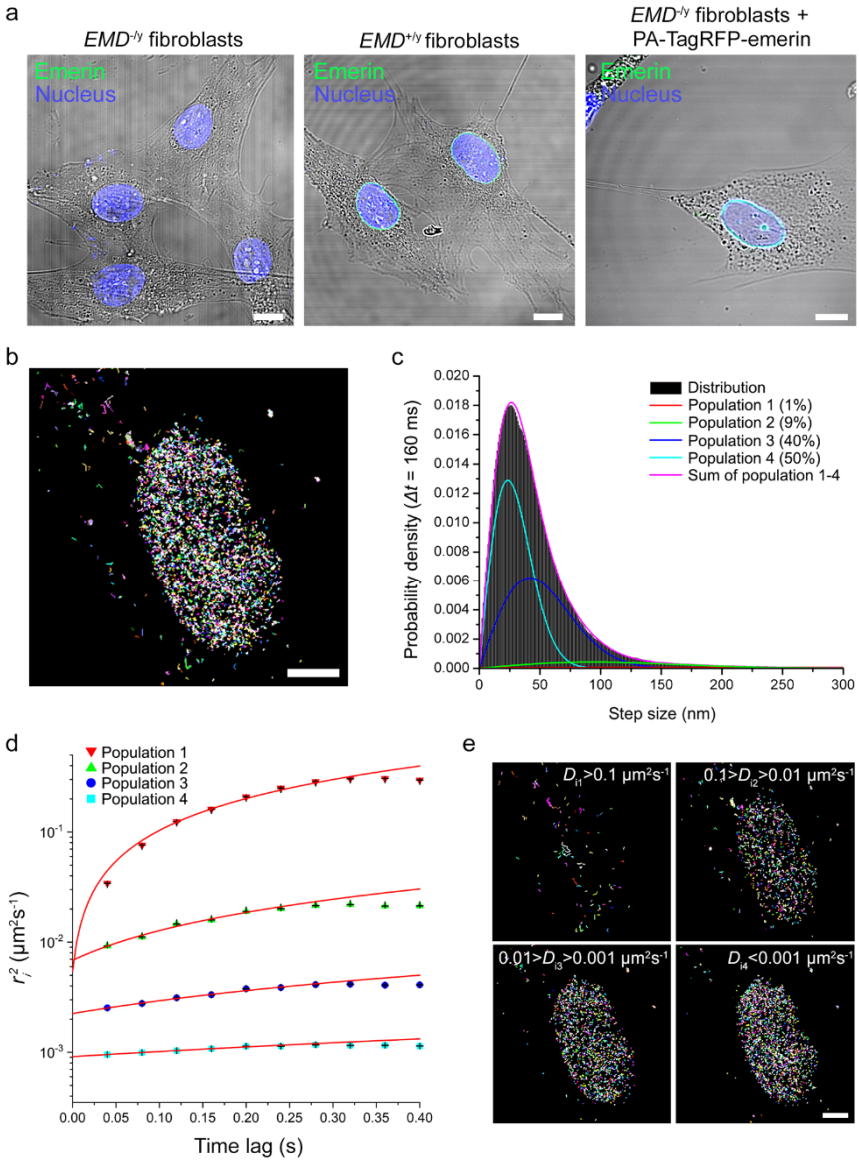

The authors declare no competing financial interests

Figure 1. **Emerin displays distinct diffusive behaviors at the nuclear envelope.** a) Immunostaining and confocal imaging of emerin in emerin-null HDF (*EMD*$^{-/y}$), HDF with endogenous emerin expression (*EMD*$^{+/y}$) and *EMD*$^{-/y}$ HDF after expression of wild-type PA-TagRFP-emerin. Scale: 10 µm. b) Map of emerin trajectories built from localization and tracking

of individual PA-TagRFP-emerin at the bottom nuclear envelope. Scale: 5 µm. c) Probability distribution of square displacement (PDSD) for wild-type emerin (71004 trajectories in 14 cells) at time lag Δt = 160 ms. The distribution is composed of four diffusive behaviors. d) Square displacement curves (r^2_i) for each emerin diffusive behavior generated from PDSD analyses on the first ten time lags Δt 40-400 ms. Curves are fitted over the first four values with a Brownian diffusion model (red line) to estimate the respective diffusion coefficients of each emerin behaviors. e) Separated emerin trajectory maps as a function of individual diffusion coefficient (D_i). Scale: 5 µm.

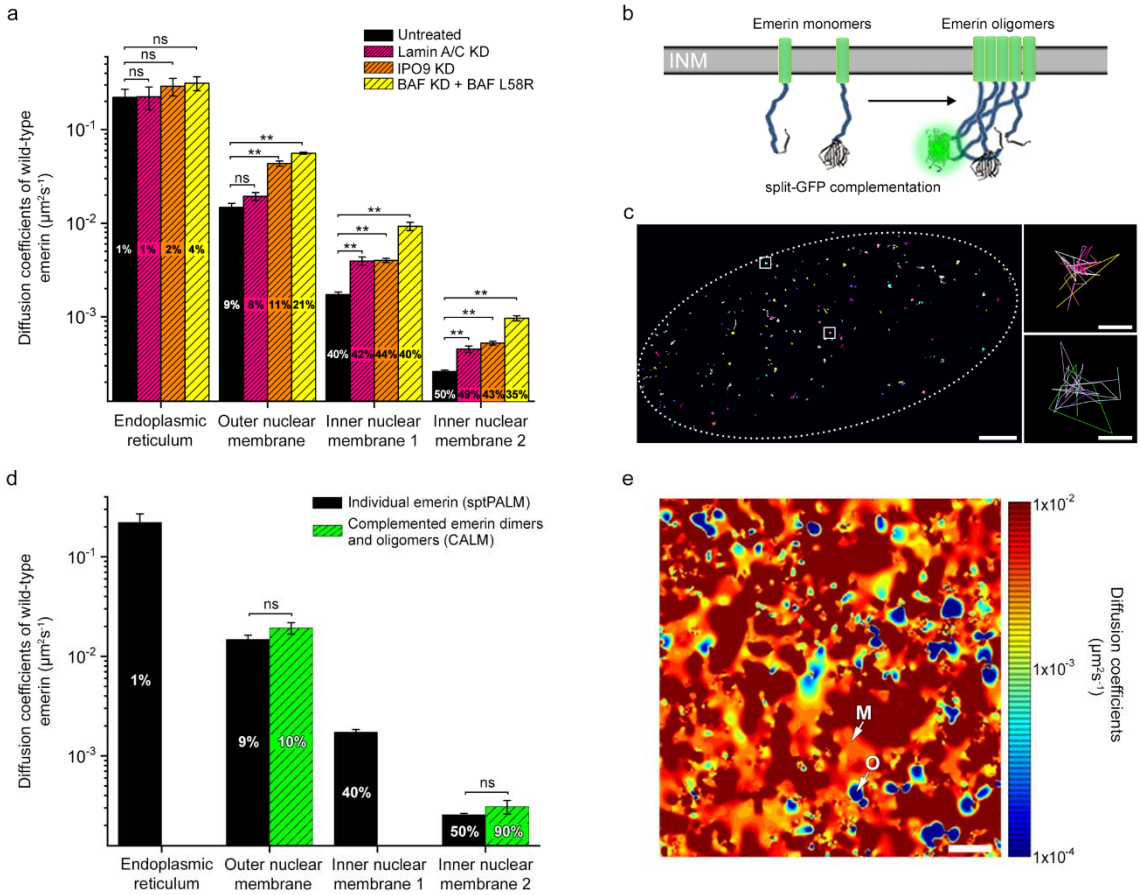

Figure 2. Emerin diffuses as inner nuclear membrane monomers and oligomers that interact with lamin A/C, nuclear actin and BAF. a) Diffusion coefficients (± s.e.m.) and population percentages of wild-type emerin (untreated, *n*=71004 trajectories in 14 nuclei) after depletion of lamin A/C (lamin A/C KD, *n*=60569 trajectories in 11 nuclei), depletion of nuclear actin (IPO9 KD, *n*=74501 trajectories in 17 nuclei) or replacement of endogenous BAF with BAF L58R mutant (BAF KD + BAF L68R, *n*=62714 trajectories in 8 nuclei) (F-test, ns: non-significant, **: $p<0.01$). b) Schematic of emerin fused to complementary split-GFP fragments and co-expressed to track the mobility of emerin oligomers by single molecule imaging of complemented GFP. c) Map of individual trajectories for complemented emerin-GFP-emerin species at the nuclear envelope (left) and examples of oligomer domains (squares) where trajectories often overlap (left). Scales: 2 µm (left) and 50 nm (right). d) Comparison of diffusion coefficients (± s.e.m.) and population percentages for individual wild-type emerin assessed by sptPALM and complemented emerin-GFP-emerin species (n=4833 trajectories in 13 nuclei) assessed by CALM (F-test, ns: non-significant). e) Diffusion map of wild-type PA-TagRFP-emerin at the nuclear envelope where emerin oligomers form slow mobility domains (blue, O) surrounded by larger areas where emerin monomers diffuse faster (red, M). Scale: 500 nm.

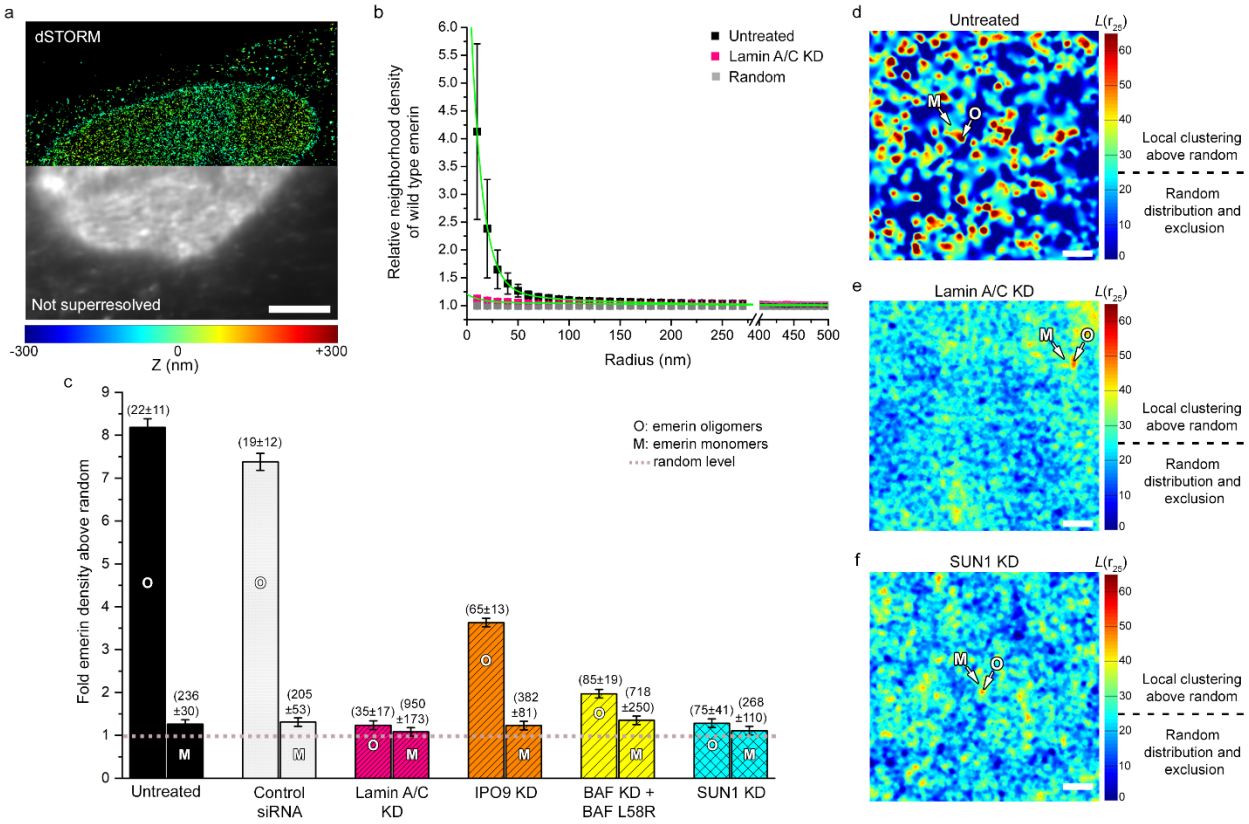

Figure 3. Emerin forms oligomeric nanodomains stabilized by lamin A/C and SUN1 and surrounded by larger emerin monomer areas across the nuclear membrane. a) Super-resolved 3D-dSTORM positions (top half) and non-super-resolved imaging (bottom half) of wild-type SNAP-emerin at the bottom nuclear envelope of an *EMD*$^{-/y}$ HDF. Scale: 5 µm. b) Neighborhood densities (± s.d.) and cluster analyses of wild-type emerin at the nuclear membrane of untreated HDF (n=189,331 localizations in 10 nuclei) and HDF after lamin A/C knock down (n=178,206 localizations in 6 nuclei). Neighborhood densities at various length scales are compared to MonteCarlo simulations of complete spatial randomness and fitted to measure molecular densities above random and length scale of significant clustering (green). c) Relative nuclear envelope molecular densities above random (± s.e.m.) for wild-type emerin oligomers (O) and monomers (M) in untreated *EMD*$^{-/y}$ HDF treated with control siRNA (n= 180,546 localizations in 5 nuclei), depleted for lamin A/C, depleted for nuclear actin after IPO9 knock down (n=225,394 localizations in 9 nuclei), with endogenous BAF replaced by BAF L58R (n=90,241 localizations in 6 nuclei) or depleted for SUN1 (n=258,300 localizations in 6 nuclei). Values in parenthesis represent the typical length scale (± s.e.m.) of each domain in nanometers. d) Local cluster map of wild-type emerin at the nuclear envelope of an untreated HDF, for a search radius of 25 nm ($L(r_{25})$). e) Local cluster map of wild-type emerin after lamin A/C knock down. f) Local cluster map of wild-type emerin after destabilization of the LINC complex by SUN1 knock down. Cluster values in maps are assigned to all localized emerin, and values $L(r_{25})$=25 represent areas where emerin is randomly distributed while $L(r_{25})$=70 values represent areas with emerin local densities $(70/25)^2$ = ~8-fold higher than expected for a random distribution. M: monomer areas, O: oligomer nanodomains. Scales for d, e and f: 250 nm.

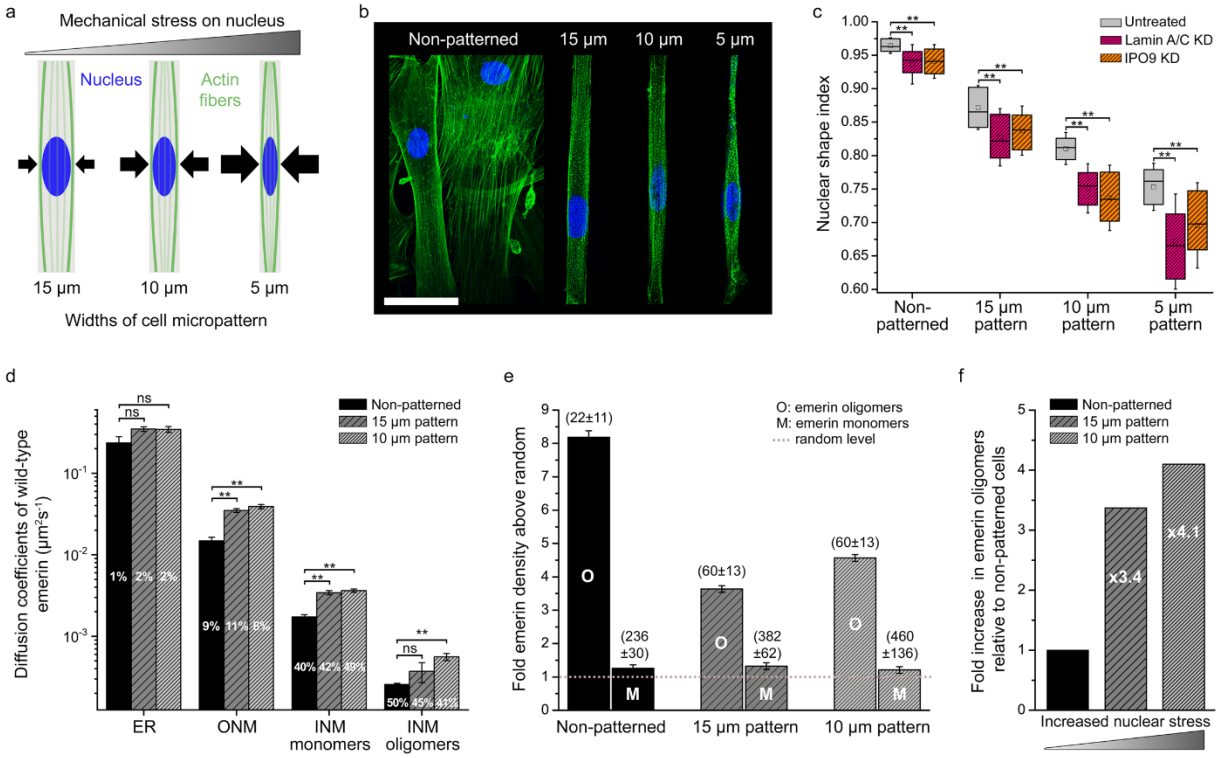

Figure 4. Mechanical stress on the nucleus increases emerin mobility and the formation of emerin oligomers. a) Schematic for increasing mechanical stress on the nucleus by cell micropatterning on rectangular fibronectin strips with decreasing widths of 15, 10 and 5 µm. Arrows represent forces. b) Fluorescence confocal imaging of actin (green) and the nucleus (blue) in micropatterned $EMD^{+/y}$ HDF. Scale: 50 µm. c) Nuclear shape index as a function of micropattern width for untreated $EMD^{+/y}$ HDF (n=54, 70, 61 and 62 nuclei for non-patterned, 15, 10 and 5 µm wide patterns, respectively), HDF depleted for lamin A/C (n=75, 60, 70 and 66 nuclei) and HDF depleted for nuclear actin (n=62, 71, 66 and 46 nuclei). Box length: index interquartile range; central square: mean; central bar: median; error bars: ± s.d. (T-test, ** $p < 0.01$). d) Diffusion coefficients (± s.e.m.) and population percentages of wild-type emerin in non-patterned cells or after nuclear deformation on 15 µm wide (n=27266 trajectories in 10 nuclei) and 10 µm wide micropatterns (n=12915 trajectories 8 nuclei) (F-test, ns: non-significant, **: p<0.01. e) Relative nuclear envelope molecular densities above random (± s.e.m.) for wild-type emerin oligomers (O) and monomers (M) in non-patterned $EMD^{-/y}$ HDF or after nuclear deformation on 15 µm wide (n=151,647 localizations in 10 nuclei) or 10 µm wide micropatterns (n=56,563 localizations in 6 nuclei). Values in parenthesis represent the typical length scale (± s.e.m.) of each domain in nanometers. f) Increase in emerin oligomers as a function of nuclear stress on 15 and 10 µm wide micropatterns compared to non-deformed nuclei in non-patterned cells.

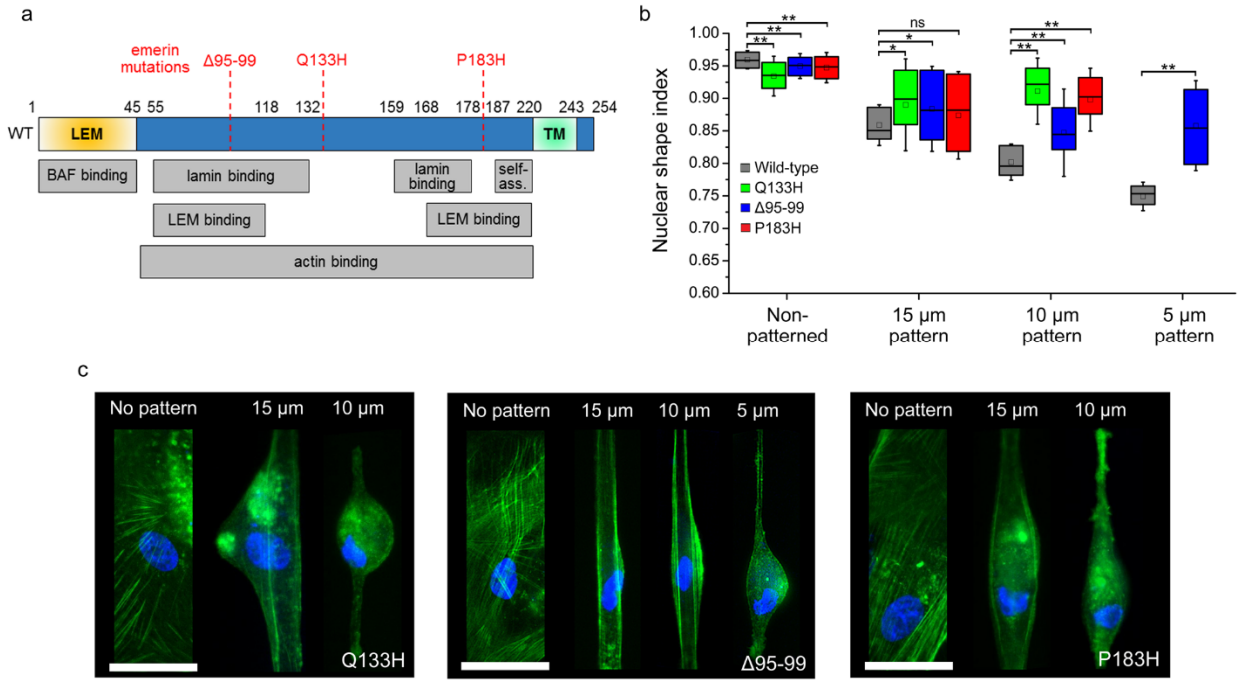

Figure 5. Emerin mutations induce defective nuclear shape adaptation against mechanical stress. a) Diagram of wild-type emerin (WT) showing its transmembrane (TM) and LEM domains, its disordered central region with relevant binding domains and self-association domain (self-ass.) and the position of Δ95-99, Q133H and P183H EDMD-inducing mutations. b) Nuclear shape index as a function of micropattern width for *EMD*$^{-/y}$ HDF expressing wild-type emerin (n=38, 33, 26 and 57 nuclei for non-patterned, 15, 10 and 5 µm wide patterns, respectively), Q133H emerin (n= 74, 58 and 37 nuclei), Δ95-99 emerin (n= 64, 89, 45 and 46 nuclei) and P183H emerin (n=82, 78 and 28 nuclei). Box length: index interquartile range; central square: mean; central bar: median; error bars: ± s.d. (T-test, ns: non-significant, *: p<0.05, **: p<0.01. c) Fluorescence wide-field imaging of actin (green) and the nucleus (blue) in micropatterned *EMD*$^{-/y}$ HDF expressing Q133H, Δ95-99 or P183H emerin mutants. Scales: 50 µm.

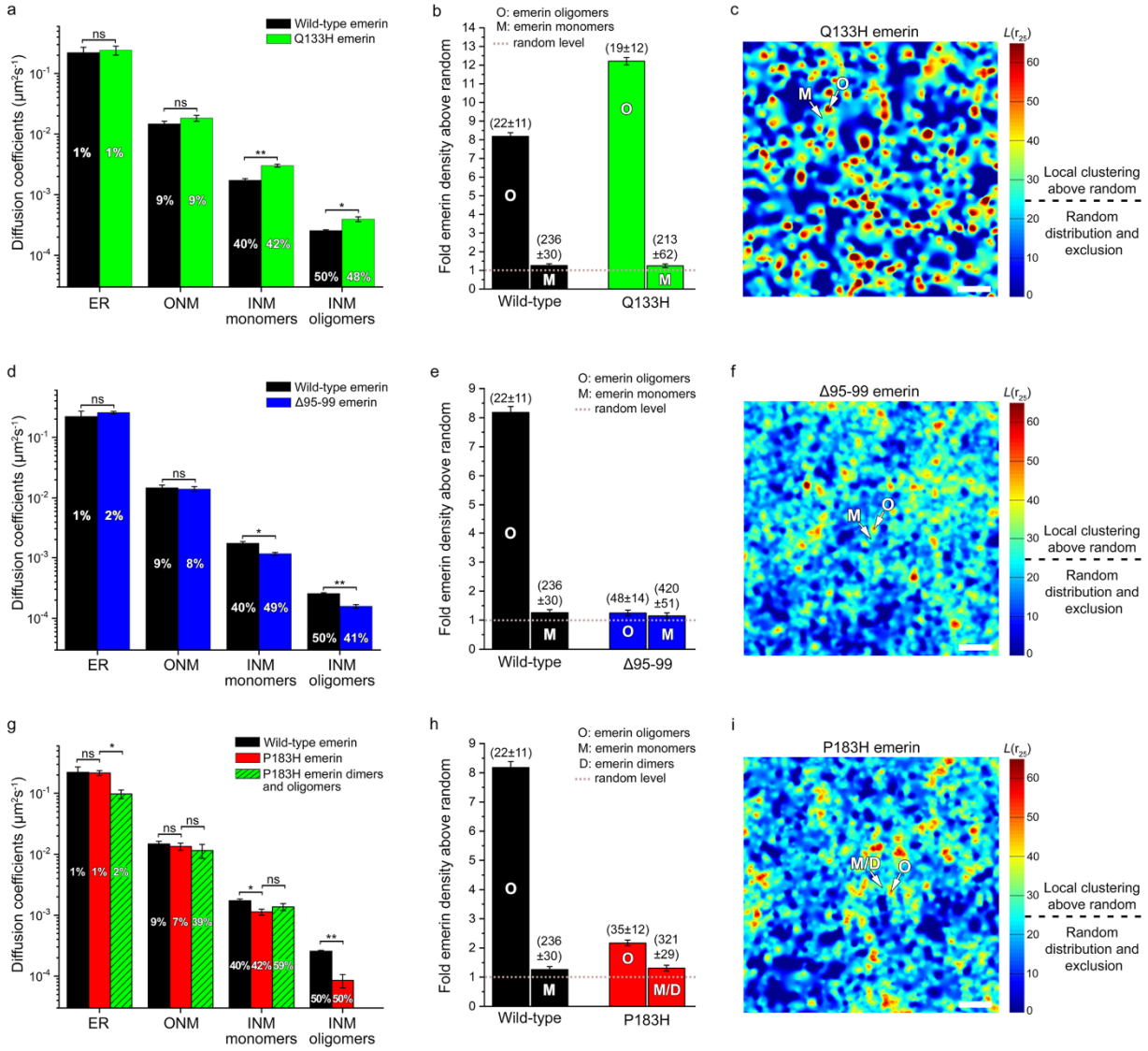

Figure 6. Emerin mutants exhibit modified lateral mobilities and defective oligomerization at the inner nuclear membrane. a) Diffusion coefficients (± s.e.m.) and population percentages of Q133H emerin (n=105050 trajectories in 13 nuclei) compared to wild-type emerin (n=71004 trajectories in 14 nuclei) (F-test, ns: non-significant, *: p<0.05, **: p<0.01). b) Relative nuclear envelope molecular densities above random (± s.e.m.) for Q133H emerin oligomers (O) and monomers (M) (n=149,340 localizations in 6 nuclei) compared to wild-type emerin (n=189,331 localizations in 10 nuclei). c) Local cluster map of Q133H emerin at the nuclear envelope for a search radius of 25 nm ($L(r_{25})$). M: monomer areas, O: oligomer nanodomains. Scale: 250 nm. d) Diffusion coefficients (± s.e.m.) and population percentages of Δ95-99 emerin (n=76944 trajectories in 14 nuclei) compared to wild-type emerin (F-test, ns: non-significant, *: p<0.05, **: p<0.01. e) Relative nuclear envelope molecular densities above random (± s.e.m.) for Δ95-99 emerin oligomers (O) and monomers (M) (n=208,092 localizations in 8 nuclei) compared to wild-type emerin. f) Local cluster map of Δ95-99 emerin. M: monomer areas, O: oligomer nanodomains. Scale: 250 nm. g) Diffusion coefficients (± s.e.m.) and population percentages of

P183H emerin (*n*=86529 trajectories in 21 nuclei) compared to wild-type emerin and compared to complemented P183H emerin-GFP-emerin species (n=10519 trajectories in 21 nuclei) assessed by CALM (F-test, ns: non-significant, *: $p<0.05$, **: $p<0.01$). h) Relative nuclear envelope molecular densities above random (± s.e.m.) for P183H emerin oligomers (O) and monomers/dimers (M/D) (n=138,075 localizations in 6 nuclei) compared to wild-type emerin. i) Local cluster map of P183H emerin. M/D: monomer/dimer areas, O: oligomer nanodomains. Scale: 250 nm. Values in parenthesis in b, e and h represent the typical length scale (± s.e.m.) of each domain in nanometers.

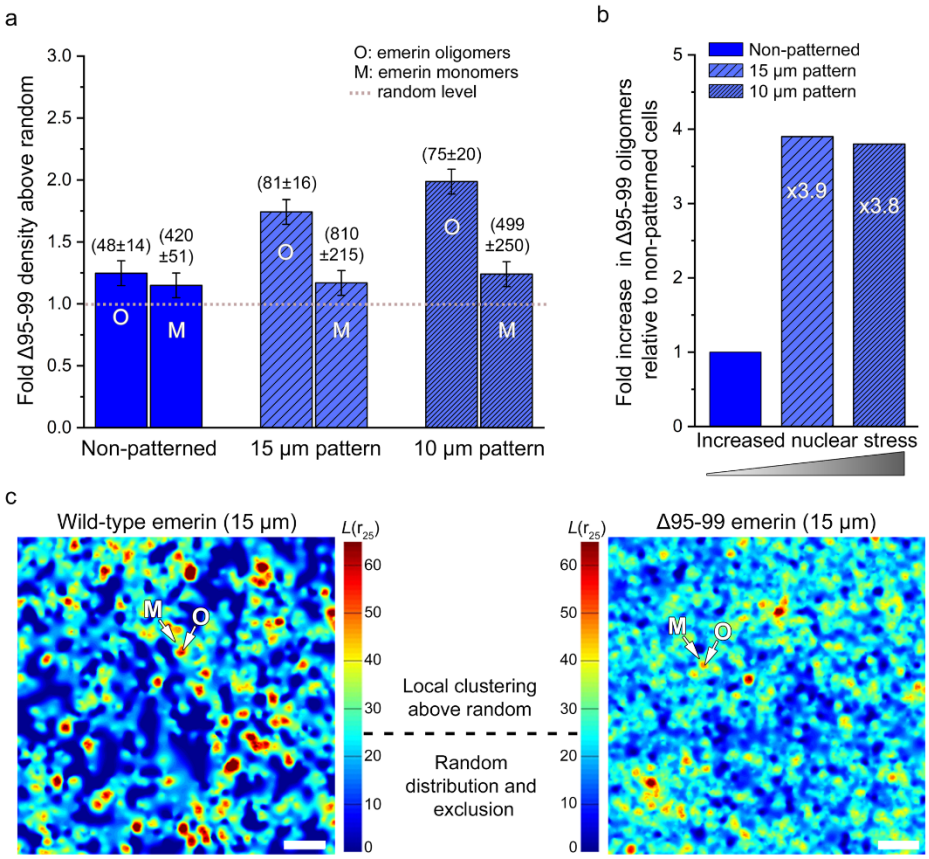

Figure 7. **Insufficient oligomerization of EDMD-inducing Δ95-99 emerin mutant against mechanical stress.** a) Relative nuclear envelope molecular densities above random (± s.e.m.) for Δ95-99 emerin oligomers (O) and monomers (M) in non-patterned *EMD*$^{-/y}$ HDF or after nuclear deformation on 15 µm wide (n=138,119 localizations in 5 nuclei) or 10 µm wide micropatterns (n=135,143 localizations in 6 nuclei). Values in parenthesis represent the typical length scale (± s.e.m.) of each domain in nanometers. b) Increase in Δ95-99 emerin oligomers as a function of nuclear stress on 15 and 10 µm wide micropatterns compared to non-deformed nuclei in non-patterned cells. c) Local cluster maps of wild-type and Δ95-99 emerin after nuclear deformation on 15 µm wide micropatterns. M: monomer areas, O: oligomer nanodomains. Scale: 250 nm.

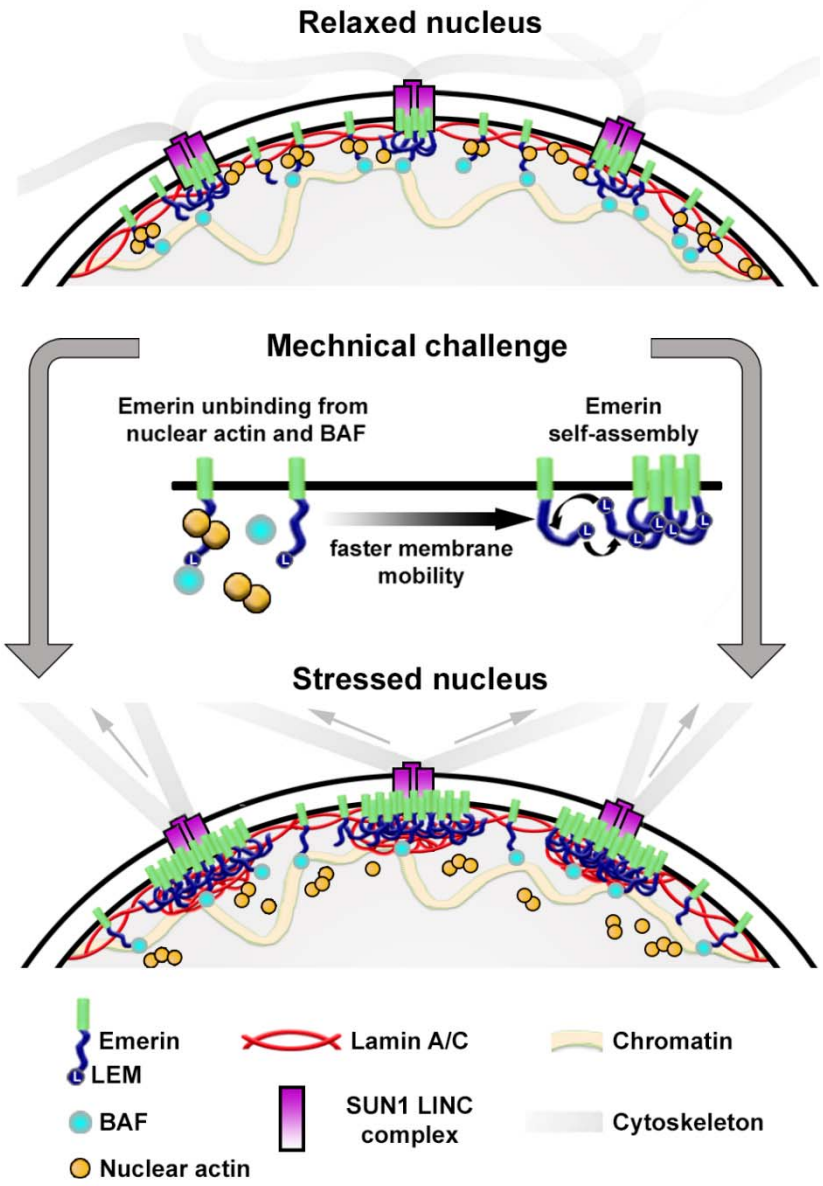

Figure 8. **Model of emerin re-organization and oligomerization at the nuclear envelope in response to mechanical challenges.** Emerin monomer unbinding from nuclear actin and BAF induces increased lateral mobility at the inner nuclear membrane and favors LEM domain interactions with binding sites along the intrinsically disordered region of other emerin, for the controlled formation of emerin oligomers at SUN1 LINC complexes and their stabilization by lamin A/C.

REFERENCES

1. Berk, J.M., Tifft, K.E. & Wilson, K.L. The nuclear envelope LEM-domain protein emerin. *Nucleus* **4**, 298-314 (2013).
2. Kirby, T.J. & Lammerding, J. Emerging views of the nucleus as a cellular mechanosensor. *Nature Cell Biology* **20**, 373-381 (2018).
3. Cui, Y. et al. Cyclic stretching of soft substrates induces spreading and growth. *Nature Communications* **6**, 6333 (2015).
4. Demmerle, J., Koch, A.J. & Holaska, J.M. The nuclear envelope protein emerin binds directly to histone deacetylase 3 (HDAC3) and activates HDAC3 activity. *The Journal of Biological Chemistry* **287**, 22080-8 (2012).
5. Stephens, A.D., Banigan, E.J., Adam, S.A., Goldman, R.D. & Marko, J.F. Chromatin and lamin A determine two different mechanical response regimes of the cell nucleus. *Molecular Biology of the Cell* **28**, 1984-1996 (2017).
6. Maurer, M. & Lammerding, J. The Driving Force: Nuclear Mechanotransduction in Cellular Function, Fate, and Disease. *Annual Review of Biomedical Engineering* **21**, 443-468 (2019).
7. Emery, A.E. Emery-Dreifuss muscular dystrophy - a 40 year retrospective. *Neuromuscular Disorders* **10**, 228-32 (2000).
8. Emery, A.E. & Dreifuss, F.E. Unusual type of benign x-linked muscular dystrophy. *J Neurol Neurosurg Psychiatry* **29**, 338-42 (1966).
9. Maggi, L., Carboni, N. & Bernasconi, P. Skeletal Muscle Laminopathies: A Review of Clinical and Molecular Features. *Cells* **5**(2016).
10. Frock, R.L. et al. Lamin A/C and emerin are critical for skeletal muscle satellite cell differentiation. *Genes & Development* **20**, 486-500 (2006).
11. Fidzianska, A. & Hausmanowa-Petrusewicz, I. Architectural abnormalities in muscle nuclei. Ultrastructural differences between X-linked and autosomal dominant forms of EDMD. *Journal of the Neurological Sciences* **210**, 47-51 (2003).
12. Park, Y.-E. et al. Nuclear changes in skeletal muscle extend to satellite cells in autosomal dominant Emery-Dreifuss muscular dystrophy/limb-girdle muscular dystrophy 1B. *Neuromuscular Disorders* **19**, 29-36 (2009).
13. Rowat, A.C., Lammerding, J. & Ipsen, J.H. Mechanical properties of the cell nucleus and the effect of emerin deficiency. *Biophysical Journal* **91**, 4649-64 (2006).
14. Lammerding, J. et al. Abnormal nuclear shape and impaired mechanotransduction in emerin-deficient cells. *Journal of Cell Biology* **170**, 781-91 (2005).
15. Yuan, J. & Xue, B. Role of structural flexibility in the evolution of emerin. *Journal of Theoretical Biology* **385**, 102-11 (2015).
16. Clements, L., Manilal, S., Love, D.R. & Morris, G.E. Direct interaction between emerin and lamin A. *Biochemical and Biophysical Research Communications* **267**, 709-14 (2000).
17. Sakaki, M. et al. Interaction between emerin and nuclear lamins. *Journal of Biochemistry* **129**, 321-7 (2001).

18. Berk, J.M. et al. The molecular basis of emerin-emerin and emerin-BAF interactions. *Journal of Cell Science* **127**, 3956-69 (2014).

19. Fairley, E.A., Kendrick-Jones, J. & Ellis, J.A. The Emery-Dreifuss muscular dystrophy phenotype arises from aberrant targeting and binding of emerin at the inner nuclear membrane. *Journal of Cell Science* **112 (Pt 15)**, 2571-82 (1999).

20. Lee, K.K. et al. Distinct functional domains in emerin bind lamin A and DNA-bridging protein BAF. *Journal of Cell Science* **114**, 4567-73 (2001).

21. Mislow, J.M.K. et al. Nesprin-1α self-associates and binds directly to emerin and lamin A in vitro. *FEBS Letters* **525**, 135-140 (2002).

22. Haque, F. et al. Mammalian SUN protein interaction networks at the inner nuclear membrane and their role in laminopathy disease processes. *Journal of Biological Chemistry* **285**, 3487-98 (2010).

23. Herrada, I. et al. Muscular Dystrophy Mutations Impair the Nuclear Envelope Emerin Self-assembly Properties. *ACS Chemical Biology* **10**, 2733-42 (2015).

24. Samson, C. et al. Emerin self-assembly mechanism: role of the LEM domain. *FEBS Journal* **284**, 338-352 (2017).

25. Roberts, R.C. et al. The Emery-Dreifuss muscular dystrophy associated-protein emerin is phosphorylated on serine 49 by protein kinase A. *FEBS Journal* **273**, 4562-75 (2006).

26. Berk, J.M. et al. O-Linked beta-N-acetylglucosamine (O-GlcNAc) regulates emerin binding to barrier to autointegration factor (BAF) in a chromatin- and lamin B-enriched "niche". *Journal of Biological Chemistry* **288**, 30192-209 (2013).

27. Guilluy, C. et al. Isolated nuclei adapt to force and reveal a mechanotransduction pathway in the nucleus. *Nature Cell Biology* **16**, 376-81 (2014).

28. Hirano, Y. et al. Dissociation of Emerin from Barrier-to-autointegration Factor Is Regulated through Mitotic Phosphorylation of Emerin in a Xenopus Egg Cell-free System*. *Journal of Biological Chemistry* **280**, 39925-39933 (2005).

29. Yates, J.R. & Wehnert, M. The Emery-Dreifuss Muscular Dystrophy Mutation Database. *Neuromuscular Disorders* **9**, 199 (1999).

30. Ellis, J.A., Craxton, M., Yates, J.R. & Kendrick-Jones, J. Aberrant intracellular targeting and cell cycle-dependent phosphorylation of emerin contribute to the Emery-Dreifuss muscular dystrophy phenotype. *Journal of Cell Science* **111 (Pt 6)**, 781-92 (1998).

31. Holt, I., Clements, L., Manilal, S. & Morris, G.E. How does a g993t mutation in the emerin gene cause Emery-Dreifuss muscular dystrophy? *Biochemical and Biophysical Research Communications* **287**, 1129-33 (2001).

32. Fernandez, A., Bautista, M., Stanciauskas, R., Chung, T. & Pinaud, F. Cell-Shaping Micropatterns for Quantitative Super-Resolution Microscopy Imaging of Membrane Mechanosensing Proteins. *ACS Applied Materials & Interfaces* **9**, 27575-27586 (2017).

33. Talkop, U.A. et al. Early onset of cardiomyopathy in two brothers with X-linked Emery-Dreifuss muscular dystrophy. *Neuromuscul Disord* **12**, 878-81 (2002).

34. Bautista, M., Fernandez, A. & Pinaud, F. A Micropatterning Strategy to Study Nuclear Mechanotransduction in Cells. *Micromachines (Basel)* **10**(2019).

35. Tokunaga, M., Imamoto, N. & Sakata-Sogawa, K. Highly inclined thin illumination enables clear single-molecule imaging in cells. *Nature Methods* **5**, 159-61 (2008).

36. Schutz, G.J., Schindler, H. & Schmidt, T. Single-molecule microscopy on model membranes reveals anomalous diffusion. *Biophysical Journal* **73**, 1073-80 (1997).

37. Ostlund, C., Ellenberg, J., Hallberg, E., Lippincott-Schwartz, J. & Worman, H.J. Intracellular trafficking of emerin, the Emery-Dreifuss muscular dystrophy protein. *Journal of Cell Science* **112 (Pt 11)**, 1709-19 (1999).

38. Dopie, J., Skarp, K.P., Rajakyla, E.K., Tanhuanpaa, K. & Vartiainen, M.K. Active maintenance of nuclear actin by importin 9 supports transcription. *Proceedings of the National Academy of Sciences of the United States of America* **109**, E544-52 (2012).

39. Cabantous, S., Terwilliger, T.C. & Waldo, G.S. Protein tagging and detection with engineered self-assembling fragments of green fluorescent protein. *Nature Biotechnology* **23**, 102-107 (2005).

40. Pinaud, F. & Dahan, M. Targeting and imaging single biomolecules in living cells by complementation-activated light microscopy with split-fluorescent proteins. *Proceedings of the National Academy of Sciences* **108**, E201-E210 (2011).

41. Iino, R., Koyama, I. & Kusumi, A. Single Molecule Imaging of Green Fluorescent Proteins in Living Cells: E-Cadherin Forms Oligomers on the Free Cell Surface. *Biophysical Journal* **80**, 2667-2677 (2001).

42. Samson, C. et al. Structural analysis of the ternary complex between lamin A/C, BAF and emerin identifies an interface disrupted in autosomal recessive progeroid diseases. *Nucleic Acids Research* **46**, 10460-10473 (2018).

43. Burger, M., Schmitt-Koopmann, C. & Leroux, J.-C. DNA unchained: two assays to discover and study inhibitors of the DNA clustering function of barrier-to-autointegration factor. *Scientific Reports* **10**, 12301 (2020).

44. Shimi, T. et al. Dynamic interaction between BAF and emerin revealed by FRAP, FLIP, and FRET analyses in living HeLa cells. *Journal of Structural Biology* **147**, 31-41 (2004).

45. Samwer, M. et al. DNA Cross-Bridging Shapes a Single Nucleus from a Set of Mitotic Chromosomes. *Cell* **170**, 956-972 e23 (2017).

46. Sengupta, P. et al. Probing protein heterogeneity in the plasma membrane using PALM and pair correlation analysis. *Nature Methods* **8**, 969-75 (2011).

47. Getis, A. & Franklin, J. Second-Order Neighborhood Analysis of Mapped Point Patterns. *Ecology* **68**, 473-477 (1987).

48. Haque, F. et al. SUN1 interacts with nuclear lamin A and cytoplasmic nesprins to provide a physical connection between the nuclear lamina and the cytoskeleton. *Mol Cell Biol* **26**, 3738-51 (2006).

49. Crisp, M. et al. Coupling of the nucleus and cytoplasm: role of the LINC complex. *J Cell Biol* **172**, 41-53 (2006).

50. Bone, C.R., Tapley, E.C., Gorjánácz, M. & Starr, D.A. The Caenorhabditis elegans SUN protein UNC-84 interacts with lamin to transfer forces from the cytoplasm to the nucleoskeleton during nuclear migration. *Mol Biol Cell* **25**, 2853-65 (2014).

51. Padmakumar, V.C. et al. The inner nuclear membrane protein Sun1 mediates the anchorage of Nesprin-2 to the nuclear envelope. *J Cell Sci* **118**, 3419-30 (2005).

52. Lei, K. et al. SUN1 and SUN2 play critical but partially redundant roles in anchoring nuclei in skeletal muscle cells in mice. *Proc Natl Acad Sci U S A* **106**, 10207-12 (2009).

53. Lu, W. et al. Sun1 forms immobile macromolecular assemblies at the nuclear envelope. *Biochim Biophys Acta* **1783**, 2415-26 (2008).

54. Hennen, J., Saunders, C.A., Mueller, J.D. & Luxton, G.W.G. Fluorescence fluctuation spectroscopy reveals differential SUN protein oligomerization in living cells. *Mol Biol Cell* **29**, 1003-1011 (2018).

55. Arsenovic, P.T. et al. Nesprin-2G, a Component of the Nuclear LINC Complex, Is Subject to Myosin-Dependent Tension. *Biophys J* **110**, 34-43 (2016).

56. Baarlink, C. et al. A transient pool of nuclear F-actin at mitotic exit controls chromatin organization. *Nat Cell Biol* **19**, 1389-1399 (2017).

57. Holaska, J.M., Kowalski, A.K. & Wilson, K.L. Emerin caps the pointed end of actin filaments: evidence for an actin cortical network at the nuclear inner membrane. *PLoS Biology* **2**, E231 (2004).

58. Bengtsson, L. & Wilson, K.L. Multiple and surprising new functions for emerin, a nuclear membrane protein. *Current Opinion in Cell Biology* **16**, 73-9 (2004).

59. Ho, C.Y., Jaalouk, D.E., Vartiainen, M.K. & Lammerding, J. Lamin A/C and emerin regulate MKL1–SRF activity by modulating actin dynamics. *Nature* **497**, 507-511 (2013).

60. Tifft, K.E., Bradbury, K.A. & Wilson, K.L. Tyrosine phosphorylation of nuclear-membrane protein emerin by Src, Abl and other kinases. *Journal of Cell Science* **122**, 3780-90 (2009).

61. Jahed, Z. et al. Molecular Insights into the Mechanisms of SUN1 Oligomerization in the Nuclear Envelope. *Biophys J* **114**, 1190-1203 (2018).

62. Schreiner, S.M., Koo, P.K., Zhao, Y., Mochrie, S.G.J. & King, M.C. The tethering of chromatin to the nuclear envelope supports nuclear mechanics. *Nature Communications* **6**, 7159 (2015).

63. Stoynova, L., Solórzano, R. & Collins, E.D. Generation of large deletion mutants from plasmid DNA. *Biotechniques* **36**, 402-4, 406 (2004).

64. Schneider, C.A., Rasband, W.S. & Eliceiri, K.W. NIH Image to ImageJ: 25 years of image analysis. *Nature Methods* **9**, 671-5 (2012).

65. Versaevel, M., Grevesse, T. & Gabriele, S. Spatial coordination between cell and nuclear shape within micropatterned endothelial cells. *Nature Communications* **3**, 671 (2012).

66. Serge, A., Bertaux, N., Rigneault, H. & Marguet, D. Dynamic multiple-target tracing to probe spatiotemporal cartography of cell membranes. *Nature Methods* **5**, 687-94 (2008).

67. Thompson, R.E., Larson, D.R. & Webb, W.W. Precise nanometer localization analysis for individual fluorescent probes. *Biophysical Journal* **82**, 2775-83 (2002).

68. Wolter, S. et al. rapidSTORM: accurate, fast open-source software for localization microscopy. *Nature Methods* **9**, 1040-1 (2012).

69. Pengo, T., Holden, S.J. & Manley, S. PALMsiever: a tool to turn raw data into results for single-molecule localization microscopy. *Bioinformatics* **31**, 797-8 (2015).

70. Perry, G.L.W. SpPack: spatial point pattern analysis in Excel using Visual Basic for Applications (VBA). *Environmental Modelling & Software* **19**, 559-569 (2004).